Terrain-adaptive motion planner for articulated construction vehicles in unstructured environments

Terrain-adaptive motion planner for articulated construction vehicles in unstructured environments

Tengchao Huang [a], Xuanwei Chen [a], Huosheng Hu [b], Shuang Song [a], Guifang Shao [a], Qingyuan Zhu [a]

[a] Pen-Tung Sah Institute of Micro-Nano Science and Technology, Xiamen University, Xiamen 361102, China
[b] School of Computer and Electronics Engineering, University of Essex, University of Essex, Colchester CO4 3SQ, UK

A B S T R A C T

In this paper, a terrain-adaptive motion planner is developed specifically for articulated construction vehicles (ACVs) to address instability issues caused by elevation changes on unstructured construction sites—challenges that traditional 2D motion planners struggle to manage effectively. The proposed planner adopts a modular framework, incorporating a terrain elevation model, an articulated vehicle kinematic model, and a posture response model. These models collaboratively capture the dynamic interactions between the vehicle and the terrain. The planner utilizes a multi-objective evaluation function to enhance the vehicle's 3D motion stability, especially in challenging terrains. By considering real-time vehicle-terrain interactions, this function estimates and optimizes the vehicle's stability. The planner's effectiveness is validated through field tests with a scaled- down ACV prototype, demonstrating significant improvements in stability and confirming its potential for practical application on unstructured terrains.

Keywords:
Articulated construction vehicles; Motion planning ; State estimation; Stable motion trajectories; Unstructured environments

1. Introduction

Articulated construction vehicles (ACVs) like loaders, dump trucks, and graders are designed with highly manoeuvrable articulated chassis, enabling them to operate effectively in complex construction sites [1]. However, these vehicles often face disturbances from uneven terrain [2], necessitating advanced motion planners to manage the challenges of large-scale construction projects [3,4]. Existing motion planners for autonomous vehicles, like map-based [5,6], model-based [7,8], and sampling-based methods [9,10], primarily focus on ensuring smooth motion trajectories in 2D structured road scenarios. These planners are inadequate for addressing the instability risks ACVs encounter in 3D unstructured terrains [11,12]. For example, in rugged environments such as ravines and slopes, the uneven ground can cause the front and rear bodies of an ACV to twist due to the differential contact of the tires. During large-angle avoidance manoeuvres, this torsion can destabilize the vehicle's centre of gravity, leading to rollover and loss of control accidents, as shown in Fig. 1.

To enhance motion planning capabilities for vehicles in unstructured terrains, current research is progressing along two main paths: map-guided and rule-constrained approaches. Map-guided planners use detailed 3D terrain representations from high-definition maps [13], cost maps [14], or digital elevation maps (DEMs) [15] to devise efficient global search and sampling strategies [16]. Rule-constrained planning, meanwhile, parameterizes the relationship between 3D terrain variables (e.g., potential fields and slopes) and vehicle dynamic variables to create rule constraints for smooth 3D trajectories [17,18]. While both approaches provide valuable insights for improving ACV stability in unstructured terrains, they have notable limitations. Map-guided planners, despite their detailed spatial representation, lack effective mechanisms to assess instability risks arising from vehicle-terrain interactions. Conversely, rule-constrained approaches, due to the complexity of their parameterized functions, often reduce vehicle representation to a single point, prioritizing smooth point-to-point movement over the stability of the vehicle's driving posture.

Motion planning methods based on the dynamic window approach (DWA) have shown notable advantages in representing the relationship between vehicles and their environment maps [19]. These methods successfully integrate vehicle parameters, kinematic constraints, and environmental data to sample feasible motion states, enabling the planner to account for vehicle heading and movement trends over time, thus improving responsiveness to dynamic environments [20].

Fig. 1. Typical unstable driving accidents of ACVs.

However, DWA's inherent focus on 2D space limits its ability to manage the complexities of 3D motion dynamics, such as elevation changes, vehicle posture, and stability. To overcome these limitations, further research is needed to adapt DWA-based methods for 3D applications, allowing them to manage the complexity of unstructured terrains and dynamic vehicle-terrain interactions in 3D space.

Unlike conventional vehicles, ACVs utilize independent front suspensions and specialized swing-rod rear suspensions, allowing different pivoting within the vertical plane for uniform tire contact and enhanced drive performance [21,22]. Stable motion planning for ACVs must address complex challenges posed by unstructured terrain and variable vehicle structures [23]. These challenges are due to the complicated motion characteristics and spatial occupancy relationships caused by the variability of vehicle structures and terrain randomness, which current map-based 3D terrain features fail to effectively associate with ACV motion posture. Additionally, the discrete continuity in 3D space of articulated vehicle bodies demands high-dimensional stability solutions, which current planners with low-dimensional smooth constraints cannot adequately provide.

To address these challenges, we propose a motion planner that integrates terrain excitation and vehicle posture response to ensure stable motion trajectories for ACVs on unstructured terrain. Building upon the dynamic planning framework of the DWA, the planner further extends a simultaneous solving mechanism that correlates vehicle posture with terrain excitation, addressing the complex motion characteristics and spatial representations that traditional ACV motion planning struggles to accommodate. Furthermore, we incorporate quantifiable 3D posture stability evaluations into the traditional evaluation function to strengthen the stability constraints for the discrete spatial representation of ACVs motion. By employing normalized weight allocation, we re-establish a dynamic balance across multiple objective functions, yielding a highly stable solution for ACV motion. The main contributions of this work can be summarized here:

- A simplified ACV posture estimation method is proposed to streamline the correlations between terrain elevation, vehicle posture, and motion retrieval, which is based on the geometric contact between tires and terrain.
- A multi-objective evaluation function has been redefined to dynamically coordinate the reasonable proportion of constraints across different dimensions, addressing the directional assessment of ACV motion states.
- A systematic planner framework with vehicle-terrain responses is designed to coordinate the orderly interaction of variables during planning iterations for supporting high-dynamic updates in motion planning.
- Extensive field experiments to verify the effectiveness of the proposed planner.

Overall, this paper proposes a systematic planner design approach by resolving the complex relationship between ACVs and unstructured terrain, aiming to provide a promising solution for achieving more stable and safer operations of ACVs under challenging terrain conditions. The rest of the paper is structured as follows. Section 2 reviews related work on advanced planner. The methodology of the proposed planner is detailed in Section 3. Section 4 details the implementation of the field experiments. Section 5 presents a comprehensive analysis of the performance metrics and effectiveness of the proposed planner through experimental validation. Finally, a brief conclusion and future work are given in Section 6.

2. Related work

The primary objective of motion planning is to design trajectories that meet predetermined goals within explicit constraints [24,25]. This is particularly challenging for ACVs, as they must maintain prominent levels of manoeuvrability and stability over unstructured terrains filled with uncertainties. Consequently, the motion planning of ACVs requires planners to accurately characterize the coupling between the vehicle and the terrain, as well as to implement trajectory inference within an expressible solution model. This section provides a detailed analysis of the related work in terms of three aspects.

2.1. Planning research for construction scenarios

The diversity of engineering tasks requires vehicle planners to possess high adaptability and flexibility, enabling them to consider environmental constraints thoroughly and design targeted execution plans. For instance, in indoor construction scenarios, Chen et al. developed a global path planning (GPP) system based on building information model (BIM) and a physical engine to address the needs of indoor inspections, effectively facilitating efficient planning in multi-obstacle environments [26,27]. Similarly, Zhu et al., guided by BIM, crafted planning strategies linked with robotic construction action nodes to optimize the execution of construction tasks [28]. Guided by the map information from BIM, these methods effectively integrated the interaction between vehicles and the environment, significantly enhancing operational efficiency in construction scenarios.

In outdoor scenarios, Kim et al. considered the environmental constraints and accessibility of excavators and dump trucks, developing a comprehensive coverage path planning algorithm to guide the autonomous operations [29]. Wang et al., focusing on the dynamic characteristics of articulated loaders, designed a path planning method guided by precise coordinates of operational targets, significantly enhancing the accuracy of the execution paths [30]. These methods, leveraging mature 2D navigation maps, have seen initial applications on flat terrains. However, in unstructured terrain with unclear road boundaries and complex terrain elevations, 2D maps struggle to provide the specific 3D navigation capabilities akin to BIM. Therefore, the foundation for autonomous planning in unstructured construction scenarios is the establishment of a 3D navigation map that can accurately represent terrain features.

2.2. 3D navigation map

As environmental perception technology advances, computer vision

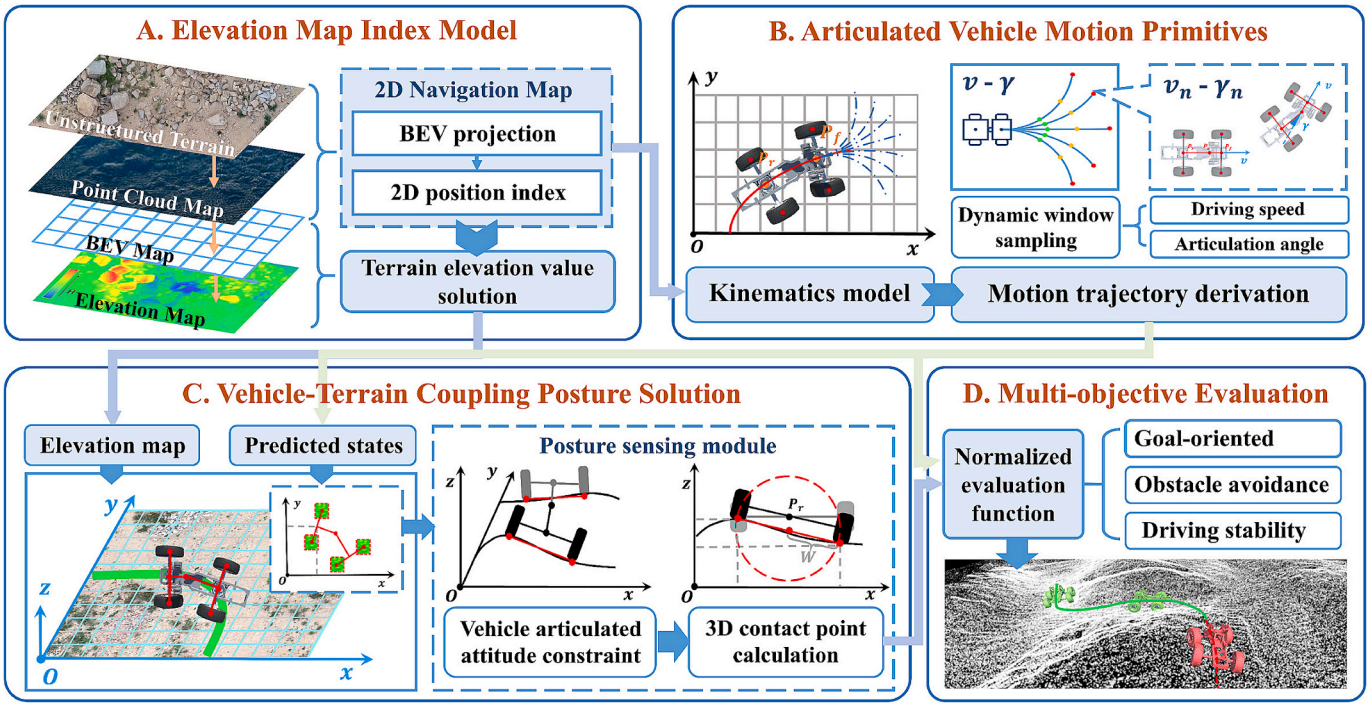

Fig. 2. Overall framework.

researchers are enhancing the representational capabilities of terrain maps to better meet the demands of vehicle navigation. Lee et al. made substantial contributions by identifying uneven road areas within 3D images, which provides essential constraints for vehicle obstacle avoidance planning [31]. Xue et al. [32] and Waibel et al. [33] effectively segmented vehicle passable regions by applying local convexity criteria to terrain point clouds. This approach enables the identification of areas that are safe for vehicle passage based on the terrain's shape and form. Cai et al. improved the multi-dimensional representation of maps by integrating semantic, elevation, and occupancy grid data, creating a real-time navigation map. This integration significantly enhances the efficiency of planners in processing unstructured environments [34].

Although these approaches effectively utilize the 3D features of terrain, they often overlook the strain responses of vehicles as they navigate through varying terrains. Consequently, navigation maps currently lack effective indexing mechanisms that would help planners assess the risks associated with unstable driving conditions caused by changes in terrain elevation. Addressing this gap is crucial. Fully leveraging map information to predict and assess vehicle responses to different terrains would enable planners to better adapt to these variations. Such advancements would ensure more stable and safer vehicle navigation, particularly in unstructured or unpredictable environments.

2.3. *Planner solution for 3D map*

Currently, motion planners capable of integrating 3D map information predominantly employ four foundational approaches: graph search-based, sampling-based, optimization-based, and model-based strategies, which are outlined below.

In graph search, Toscano-Moreno et al. introduced the DEM-AIA planning scheme, addressing constraints related to off-road vehicle tilt and terrain slope features [35]. Liu et al. developed the T-Hybrid A* search method to optimize motion trajectories on 2.5D maps [36]. These methods tend to design optimal trajectories at a regional global level, which results in overlooking immediate vehicle state constraints and fails to meet the demands of ACVs for stable driving postures in detail.

In sampling-based approaches, Ji et al. proposed an RRT solution based on OctoMap to improve adaptivity to 3D vehicle motion [37], and Endo et al. expanded the CL-RRT algorithm with the BenchNav method to enhance traversability in 3D terrains [38]. Although they focused on local map details as graph search-based methods did, their insensitivity to vehicle states makes it challenging for ACVs to overcome terrain disturbances.

Optimization-based methods focus on improving the smoothness of local trajectories. Hu et al. utilized nonlinear optimal control to define motion costs for differential steering vehicles, integrating these into an artificial potential field function (APF) that accounts for terrain and obstacles [39]. Chen et al. proposed the tracking error boundary (TEB) to enhance adaptability to terrain disturbances [40]. While these approaches effectively optimize 3D trajectories by incorporating environmental parameters and vehicle dynamics, they often simplify vehicles to vector points to maintain solution efficiency. This simplification can prioritize smoothness over the stability of autonomous and connected vehicles' (ACVs) driving postures, potentially overlooking critical aspects of vehicle stability in detailed scenarios.

Model-based methods effectively incorporate vehicle state prediction in representing driving posture details. Qi proposed a hierarchical planning framework based on this concept, integrating spline-based optimization and motion smoothness constraints deeply with the sensitivity of DWA to vehicle motion states [41]. Yao explored a state-energy graph based on motion primitives to constrain kinetic smoothness of motion trajectories [42]. Chen et al. linked 3D terrain semantic perception with DWA and designed RSPMP to achieve good results in local path planning [43]. Although these methods could effectively implement planning by combining vehicle status predictions in 2D map, their insensitivity to 3D space results in numerous limitations when applied to ACVs.

Overall, current motion planners have made some progress in managing smooth motion planning of vehicles on unstructured terrains, but further research and improvement are needed to simultaneously optimize trajectories while ensuring stable motion postures.

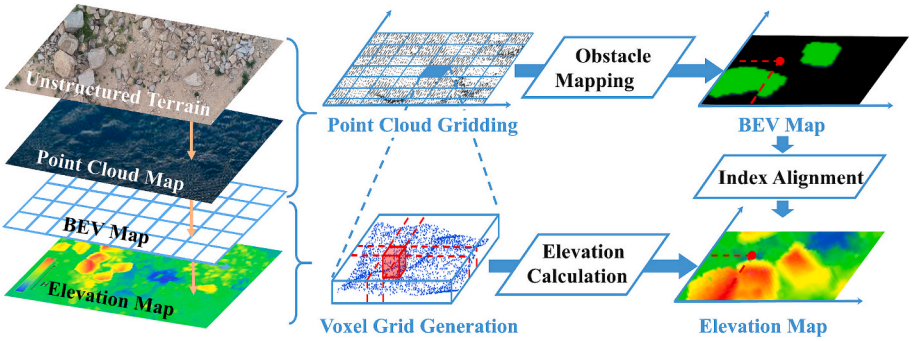

Fig. 3. Modelling process for multi-layer maps.

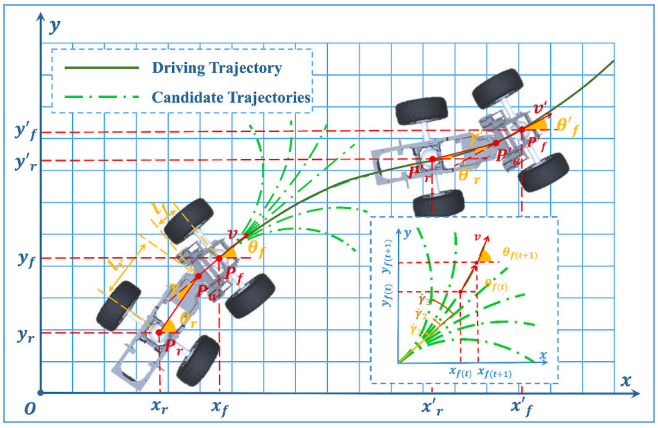

Fig. 4. Kinematic primitives of an articulated vehicle.

3. Methodology

3.1. Overall framework

Fig. 2 shows the overall framework for our proposed planner that comprises four main components: elevation map index model, articulated vehicle motion primitives, vehicle-terrain coupling posture solution, and multi-objective evaluation. Initially, an integrated 2D grid navigation map and an elevation index model are developed based on a multi-layer digital map framework to address the standardization of discrete structures in 3D terrain point clouds. Concurrently, vehicle motion primitives that account for articulated steering characteristics are established, aimed at matching dynamic window sampling for trajectory derivation. Building on this foundation, a vehicle-terrain coupling module is established based on tire-ground contact relationships to solve for vehicle motion posture under terrain excitation. Finally, a multi-objective evaluation function is set up within the unified planner to achieve vehicle trajectory planning, which could balance goal orientation, obstacle avoidance, and steady-state safety.

3.2. Elevation map index model

Most maps used for autonomous vehicle planning are constructed using point cloud data gathered from sensors such as LiDAR or depth cameras, which accurately preserve 3D terrain information. However, due to the discrete and unordered nature of the 3D points, map retrieval is time-consuming. To address this, most autonomous systems employ a bird's eye view (BEV) [44], projecting 3D point clouds onto a 2D navigation map, M_{BEV}, to delineate passable areas. M_{BEV} can be represented as follows:

$$M_{BEV} = \begin{bmatrix} m_{1,1} & \cdots & m_{1,W} \\ \vdots & \ddots & \vdots \\ m_{H,1} & \cdots & m_{H,W} \end{bmatrix} \tag{1}$$

where $m_{i,j}$ represents the occupancy grid attribute. H and W denote the number of grids along the X and Y axis of the map, respectively.

Let $v_{i,j}$ denote the spatial grid at the position (i,j) on the map. Each grid corresponds to a point cloud data scale of size $h \times w$. The 2D planar area corresponding to $v_{i,j}$ is defined as

$$v_{i,j} = \{x \in [(i-1)h, ih], y \in [(i-1)w, iw] | i \in N^+, j \in N^+\} \tag{2}$$

and $m_{i,j}$ denote as:

$$m_{i,j} = \begin{cases} 0 \text{ if } v_{i,j} \text{ is passable}, \\ 1 \text{ otherwise}. \end{cases} \tag{3}$$

In our previous research [45], we proposed a method for safety semantic segmentation to assess the traversability of $v_{i,j}$. This method simplifies the marking of passable areas on the grid map by binary obstacle segmentation of terrain features that affect vehicle movement. However, the 2D map format is insufficient to represent the 3D terrain structure. To bridge the gap between these dimensions, a map model is developed based on the BEV that indexes elevation details, as shown in Fig. 3.

This model builds upon existing BEV map localization by further calculating the mean elevation using a vowelised point cloud indexed by unit area. Suppose $p_k = (x_k, y_k, z_k)$ represents the coordinates of the k-th point within a voxel. Mathematically, this model can be expressed as a discrete ordered set of a solution function, specifically:

$$f_p(x_n, y_n) = \frac{\sum_{k=1}^{NUM} z_k}{NUM}, z_k \epsilon \{p_1, p_2, \cdots, p_{NUM}\} \tag{4}$$

where f_p serves as an elevation indexing function on the BEV map at coordinates (x_n, y_n), with $n \in N^+$. NUM represents the total number of neighbouring point clouds.

Assuming the neighborhood size is defined by a grid with side length d, the relationship between the point cloud sequence and the 2D domain is as follows:

$$p_k \epsilon \left\{ (x_k, y_k) | |x_k - x_n| < \frac{d}{2}, |y_k - y_n| < \frac{d}{2} \right\} \tag{5}$$

where d is a constant value, empirically taken as half the width of a tire, approximating the contact surface between the tire and the terrain. p_k represents the coordinates within the neighborhood point clouds, and the neighborhood size is defined by a grid with side length d, empirically set to half the tire width, approximating the contact surface between the tire and the terrain.

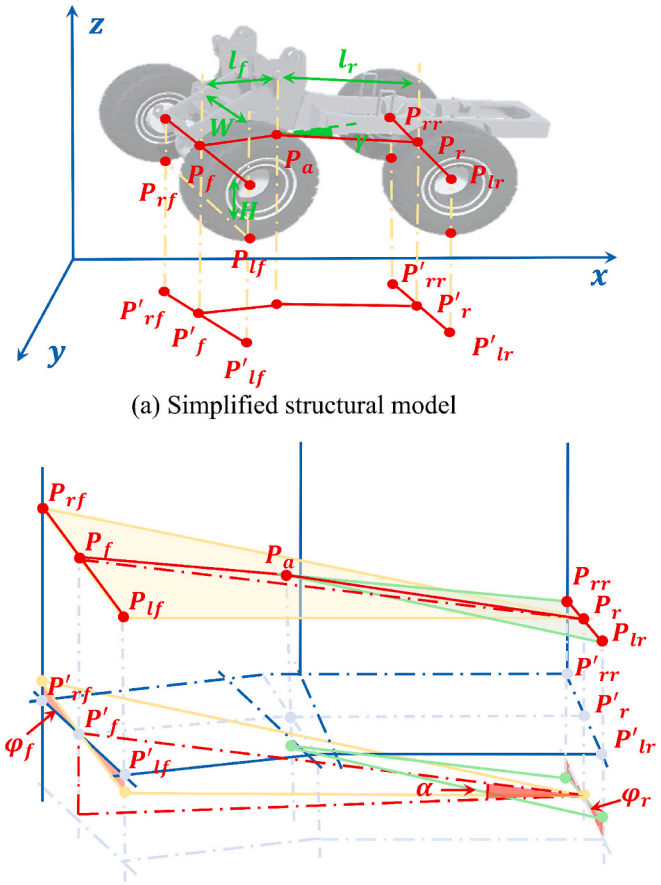

Fig. 5. Simplified ACV geometric posture model.

3.3. Articulated vehicle motion primitives

Fundamentally, vehicle motion planning involves dynamically evaluating future trajectories based on known motion states [46]. For instance, DWA utilizes a kinematics-based sampling window to calculate motion trajectories for traditional vehicles [47]. While this method is more suited for differential or omnidirectional moving vehicles, it also holds certain applicability for articulated vehicles that achieve differential steering of the front and rear tires through steering rod thrust, provided certain steering constraints are met. Therefore, constructing a vehicle kinematics model that accurately reflects the constraints of articulated steering is crucial for calculating candidate trajectories.

As illustrated in Fig. 4, the articulated vehicle achieves steering by controlling its articulation angle γ between the front and rear bodies. We represent the positions of the front and rear bodies by the midpoints of the front and rear axles, P_f and P_r, respectively. $\theta_f$and θ_r are the heading angles of the front and rear bodies relative to the coordinate system. The kinematic model can be established below:

$$\begin{cases} \dot{x}_f = v cos\theta_f \\ \dot{y}_f = v sin\theta_f \\ \dot{\theta}_f = \dfrac{v sin\gamma_t + l_r\dot{\gamma}}{l_f cos\gamma_t + l_r} \end{cases} \tag{6}$$

where v is the driving speed, $\left(\dot{x}_f, \dot{y}_f\right)$ are the velocity components of the front body in the x and y directions, and $\dot{\gamma}$ is the articulation angular velocity, with counterclockwise direction being positive.

Unlike traditional sampling spaces, the vehicle's sampling window here is $[v, \dot{\gamma}]$. Notably, as construction vehicles may experience unpredictable loss of control at high speeds due to large inertia, they typically operate at a steady low speed. In this study, we aim to maintain speed at a controllable and regular value to mitigate the risk of loss of control.

To enhance the computational efficiency of the dynamic window function, driving trajectories derived from the kinematic model are typically represented in a discretized form. Assuming a time interval of Δt, in the global coordinate system, the future trajectory points and heading postures of the front body have the following relationship:

$$\begin{cases} x_{f(t+1)} = x_{f(t)} + v cos\theta_{f(t)}\Delta t \\ y_{f(t+1)} = y_{f(t)} + v sin\theta_{f(t)}\Delta t \\ \theta_{f(t+1)} = \theta_{f(t)} + \dfrac{v sin\gamma_t + l_r\dot{\gamma}}{l_f cos\gamma_t + l_r}\Delta t \\ \gamma_{(t+1)} = \gamma_{(t)} + \dot{\gamma}\Delta t \end{cases} \tag{7}$$

The vehicle moves in a straight line when $\gamma_{(t)} = 0$ and $\dot{\gamma} = 0$. The vehicle performs a steering motion when $\gamma_{(t)} \neq 0$ or $\dot{\gamma} \neq 0$. During steering, the motion of the rear body is influenced by the front body, with steering control achieved through the articulation angle. Therefore, based on the articulation structure between the front and rear bodies of the vehicle, at any given moment t, the heading angles between the front and rear bodies of the articulated vehicle satisfy:

$$\theta_{r(t)} = \theta_{f(t)} + \gamma_{(t)} \tag{8}$$

Based on this, the 2D trajectory points of the rear body can be derived from the coordinates of the front body:

$$\begin{cases} x_{r(t)} = x_{f(t)} - l_r cos\theta_{f(t)} - l_r cos\theta_{r(t)} \\ y_{r(t)} = y_{f(t)} - l_f sin\theta_{f(t)} - l_r sin\theta_{r(t)} \end{cases} \tag{9}$$

3.4. Vehicle-terrain coupling posture solution

This section introduces a posture perception module for predicting 3D vehicle motion trends. This module is critical for vehicle-terrain interaction, with two stages: 1) Standardizing the yaw, pitch, and roll by simplifying the multi-degree-of-freedom posture of articulated bodies; 2) Implementing the multi-models coupling association and binary approximation to establish the solution relationship between the tire and ground. This module enables the planning algorithm to realize a transition from 2D to 3D space, quantifying vehicle posture changes effectively.

3.4.1. Simplified representation of ACV posture

To characterize the motion posture of ACVs, we simplify the representation of the front and rear body postures based on their rigid body characteristics. As shown in Fig. 5, this simplified linkage model involves the articulation point P_a, the front and rear axle support points P_f and P_r, and the vehicle's four-wheel contact points $[P_{lf}, P_{rf}, P_{lr}, P_{rr}]$. Additionally, to standardize posture calculations, we align the vehicle's yaw angle with the 2D heading angles θ_f and θ_r, using the actual IMU's north-east-sky (NES) coordinate system to match the map coordinates.

Assuming the radius of each tire is consistent and deformation is negligible, we define P'_a, P'_f and P'_r as the ground projections of P_a, P_f and P_r, respectively. Due to the rigid connection of the vehicle's independent front suspension, P'_a, P'_f and P'_r share a coplanar relationship with the ground contact points P_{lf} and P_{rf}. With the articulation angle γ known, the coordinates of P'_f and P'_r are $\left(x_f, y_f, z_f\right)$ and (x_r, y_r, z_r) respectively. The vehicle's pitch angle α can be expressed as the angle between the plane formed by $\triangle P_{lf}P_{rf}P'_r$ and the xy-plane.

$$\alpha = arcsin\left(\frac{z_f - z_r}{\sqrt{{l_f}^2 + {l_r}^2 + 2l_f l_r cos\gamma}}\right) \tag{10}$$

Table 1
Detailed parameters of the scale prototype.

Parameters	Unit	Value
Distance from articulated point to front axle (l_f)	m	1.68
Distance from articulated point to rear axle (l_r)	m	1.87
Half-track width (W)	m	0.29
Tire radius (R)	m	0.23
Maximum steering angle (γ)	rad	0.52
Maximum swing angle of rear body ($\Delta\varphi_{max}$)	rad	0.34
Maximum velocity (v)	$m \bullet s^{-1}$	5.00
Maximum angular velocity (ω)	$rad \bullet s^{-1}$	0.25

Additionally, as shown in Fig. 5(b), the front and rear axles can be adjusted vertically within a certain angle due to the special articulated rear suspension. Based on the ground contact relationship, the roll anglesφ_f and φ_r can be characterized by the angles between the line segments $\overline{P_{lf}P_{rf}}$ and $\overline{P_{lr}P_{rr}}$ and the xy-plane, respectively. Assuming the elevations of the four ground contact points are $[z_{lf}, z_{rf}, z_{lr}, z_{rr}]$, φ_f and φ_r can be defined as follows:

$$\begin{cases} \varphi_f = arcsin\left(\dfrac{z_{lf} - z_{rf}}{2W}\right) \\ \varphi_r = arcsin\left(\dfrac{z_{lr} - z_{rr}}{2W}\right) \end{cases} \tag{11}$$

Since P'_f and P'_r are the midpoints of $\overline{P_{lf}P_{rf}}$ and $\overline{P_{lr}P_{rr}}$ respectively, then:

$$\begin{cases} z_f = \dfrac{z_{lf} + z_{rf}}{2} \\ z_r = \dfrac{z_{lr} + z_{rr}}{2} \end{cases} \tag{12}$$

Substituting further into Eq. (10), the roll angle α can also be further expressed as:

$$\alpha = arcsin\left(\frac{z_{lf} + z_{rf} - z_{lr} - z_{rr}}{2\sqrt{{l_f}^2 + {l_r}^2 + 2l_f l_r cos\gamma}}\right) \tag{13}$$

Utilizing Eqs. (11) and (13), the roll and pitch angles of articulated vehicles are linked to the elevation indices of tire contact points, enabling further prediction of the vehicle's 3D posture changes along the predictive trajectory.

3.4.2. Approximate estimation of vehicle-terrain coupling

In this section, we construct a coupling solution module to predict the vehicle-terrain coupling posture by using the simplified structural model of ACV and the elevation index model. In this module, we introduce the posture constraints previously described, linking the four tire contact points $[P_{lf}, P_{rf}, P_{lr}, P_{rr}]$ with predictions of vehicle motion posture. Additionally, to improve the solving efficiency, we employ a binary approximation method to simplify the solution process.

To ensure consistency, we set the lookahead point as the vehicle's front axle pivot point for path planning, which is denoted as P_f. Using the kinematic equations outlined in Section 2.3, we determine the planar coordinates of P'_f and its heading θ_f along the future trajectory. Through projection relationships, we establish the symmetrical positioning of P_{lf} and P_{rf} relative to P'_f. Assuming a roll angle φ_f for the vehicle's front axle in 3D space, the 2D projection errors of the tire contact points on the ground are determined below:

$$\begin{cases} \Delta D_{fx} = \dfrac{W}{s} cos\varphi_f sin\theta_f \\ \Delta D_{fy} = \dfrac{W}{s} cos\varphi_f cos\theta_f \end{cases} \tag{14}$$

where W denotes the half-wheelbase of the vehicle, a constant value, and s represents the scaling factor aimed at standardizing the dimensions of the map and the vehicle parameters.

The 2D index coordinates of the tire contact points can further be determined below:

$$\begin{cases} \left(x_{lf}, y_{lf}\right) = \left(x_f - \Delta D_{fx}, y_f + \Delta D_{fy}\right) \\ \left(x_{rf}, y_{rf}\right) = \left(x_f + \Delta D_{fx}, y_f - \Delta D_{fy}\right) \end{cases} \tag{15}$$

By combining Eq. (4), the elevation values can be determined:

$$\begin{cases} z_{lf} = f\left(x_{lf}, y_{lf}\right) \\ z_{rf} = f\left(x_{rf}, y_{rf}\right) \end{cases} \tag{16}$$

Corresponding to Eq. (12), a correlation between map elevation indices and vehicle ground pose can be established. To address this correlation, we approximate φ_f within the range $[\varphi_{fmin}, \varphi_{fmax}]$, allowing for error ε_r. The iteration termination constraint is defined as:

$$\left| arcsin\left(\frac{f\left(x_{lf}, y_{lf}\right) - f\left(x_{rf}, y_{rf}\right)}{2W}\right) - \varphi_{f(n)} \right| < \varepsilon_r \tag{17}$$

where φ_f represents the near-optimal roll angle of the front vehicle body within the permissible error if the n-th iterated angle $\varphi_{f(n)}$ satisfies the relationship.

Given the known articulation angle γ, the heading angle θ_r of the rear vehicle body can be similarly determined. However, due to the simultaneous presence of pitch angle α and roll angle φ_r, the vehicle's rear wheel contact points, P_{lr} and P_{rr}, require calculation with the aid of the projection point of the rear axle pivot on the ground, denoted as P'_r. The coordinate relation between P'_r and P'_f is as follows:

$$\begin{cases} x_f - x_r = \left(\dfrac{l_f}{s} cos\theta_f + \dfrac{l_r}{s} cos\theta_r\right) cos\alpha \\ y_f - y_r = \left(\dfrac{l_f}{s} sin\theta_f + \dfrac{l_r}{s} sin\theta_r\right) cos\alpha \end{cases} \tag{18}$$

where the pitch angle range can be set as $[0, \alpha_{max}]$ due to the symmetry of the cosine function.

Simultaneously, with the rigid connection between the front and rear vehicle bodies, the rear wheel swing angle is based on the adjustment of $\varphi_{f(n)}$ of the front vehicle body. Referring to Eqs. (13) and (14), the coordinates of P'_{lr} and P'_{rr} under 2D projection can also be determined. Consequently, the criterion for $\varphi_{r(n)}$) is as follows:

$$\left| arcsin\left(\frac{f(x_{lr}, y_{lr}) - f(x_{rr}, y_{rr})}{2W}\right) - \varphi_{r(n)} \right| < \varepsilon_r \tag{19}$$

The maximum limit angle of the rear axle, denoted as $\Delta\varphi$, is determined through calibration experiments as described in Section 3.3 and is presented in Table 1. Therefore, the index range for the rear wheel roll angle can be defined as $[\varphi_{f(n)} - \Delta\varphi, \varphi_{f(n)} + \Delta\varphi]$. Based on the concept, the solution logic of the designed module is illustrated in Algorithm 1. To estimate the coupled posture, we employ a geometric bisection method to approximate the four-wheel contact points of an ACV, thus exploring the most probable ground poses of the vehicle relative to the terrain. We address algorithm efficiency and accuracy from three perspectives below.

- Firstly, roll and pitch angles are set to 0° as the starting point for iteration at initialization.
- Secondly, permissible error is compensated by iterating m_0 times until the difference between the solution error and index error of 1/2 falls within the range of ε_r.

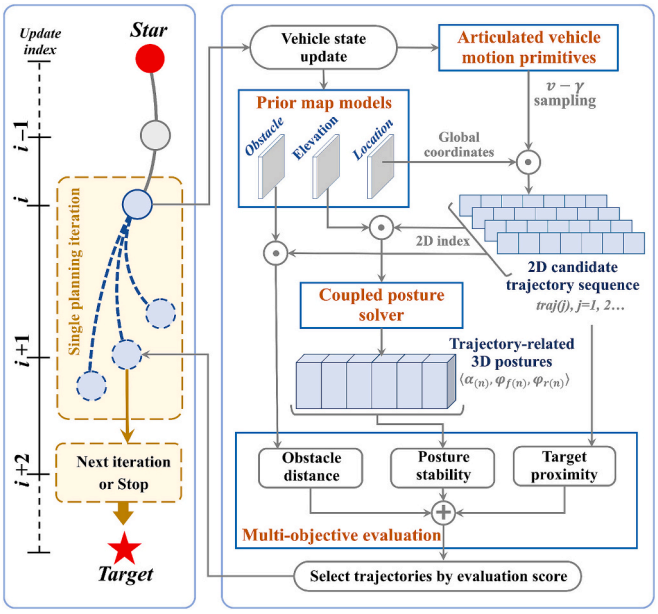

Fig. 6. Iterative planning process of the motion planner.

- Thirdly, a forward constraint function is devised for considering historical pitch angle trends to maintain consistency between the solved pose and the vehicle's forward motion pattern.

Algorithm 1Vehicle-Terrain coupling attitude solver

Function $\langle \alpha, \varphi_f, \varphi_r \rangle$=VTC-AS (DEM, P'_f, θ_f, γ):

▷ Initialization:

$g(x, y) \leftarrow$ DEM

Tolerance $\leftarrow \varepsilon_r$, Iteration $\leftarrow m_0$

▷ Establish vehicle 2D structure model:

Set constants: l_f, l_r, W

$\theta_r \leftarrow \theta_f + \gamma$

$[P'_a,\ P'_r] \leftarrow JointCalculation(P'_f, \theta_f, \gamma, l_f, l_r)$

$[P_{lf}, P_{rf}, P_{lf}, P_{rf}] \leftarrow TireCalculation(P'_f, P'_r, \theta_f, \theta_r, W)$

▷ Calculation of ground point elevation:

Set initial value: $\langle \alpha_{(0)}, \varphi_{f(0)}, \varphi_{r(0)} \rangle \leftarrow \langle 0, 0, 0 \rangle$

While n < m_0 **do**

  for each $[x_t, y_t]$ in $[P_{lf}, P_{rf}, P_{lf}, P_{rf}]$ **do**

    Set range: $P_{terrain} \leftarrow \{|x_{DEM} - x_t| < d, |y_{DEM} - y_t| < d\}$

    for $(x_i, y_i) \in P_{terrain}$ **do**

      $g_{elevation} \leftarrow Mean\ [\sum g(x_i, y_i)]$

      $[P_{Tire(n)} \cdots] \leftarrow Update3DPoint([P_{Tire(n-1)} \cdots],\ g_{elevation})$

  $\langle \alpha_{(n)}, \varphi_{f(n)}, \varphi_{r(n)} \rangle \leftarrow DeclinationEstimation([P_{Tire} \cdots], l_f, l_r, W)$

  if $\varphi_{f(n)} \notin condition1\langle \varphi_{f(n-1)}, \varepsilon_r \rangle$ **then**

    $\varphi_{f(n)} \leftarrow Bisection\langle \varphi_{f(n)}, \varphi_{f(n-1)} \rangle$

  $lim \leftarrow ForwardConstraint(P'_r, \alpha_{(n-1)})$

  if $\langle \alpha_{(n)}, \varphi_{r(n)} \rangle \notin condition2\langle lim, \alpha_{(n-1)}, \varphi_{R(n-1)}, \varepsilon_r \rangle$ **then**

    $\alpha \leftarrow Bisection\langle \alpha_{(n)}, \alpha_{(n-1)} \rangle$

    $[P_{lf}, P_{rf}] \leftarrow Recalculate\langle P'_r, \alpha \rangle$

    $\varphi_r \leftarrow DeclinationEstimation\&Bisection([P_{lf}, P_{rf}], \varphi_{f(n)}, \varphi_{f(n-1)})$

return $\langle \alpha, \varphi_f, \varphi_r \rangle$

3.5. Multi-objective evaluation function

In this section, we enhance the assessment of proximity capability and obstacle avoidance capability by considering the motion characteristics of ACVs. Simultaneously, indicators of vehicle motion stability under coupled terrain stimuli are incorporated into the evaluation function, facilitating the selection of more stable motion paths by the algorithm. The specifics of each sub-function are as follows.

Proximity capability: For articulated vehicles, the angle difference between the future heading angle of the front vehicle body and the target orientation, along with the 2D straight-line distance from the predicted trajectory to the target position, collectively determine the vehicle's capability to approach the target. We improve the projection distance to quantify the vehicle's ability to approach the target within different predicted trajectories:

$$J_{heading}(i) = \sum_{t=1}^{m} \left|\overline{P_T P_{(t)}}\right| \left|sin\left(\theta_{T(t)} - \theta_{f(t)}\right)\right| \tag{20}$$

where i denotes the trajectory number corresponding to different $\dot{\gamma}$ values, m represents the prediction step size, P_T denotes the 2D coordinates of the target point, and $P_{(t)}$ represents the 2D coordinates of the predicted position at time t. $\theta_{T(t)}$ and $\theta_{f(t)}$ respectively represent the azimuth angle from the predicted point to the target position and its own heading angle.

Obstacle avoidance capability: Due to the articulated structure of ACVs, we evaluate the obstacle avoidance capability of the predicted trajectory by defining the distance between the front and rear vehicle bodies and the nearest obstacle. Considering the simplified structure of the dual bodies, denoted as P_f and P_r, representing the 2D distances to obstacles, and setting the vehicle's safety avoidance threshold as d_{min}, the evaluation function is formulated as:

$$J_{dist}(i) = \sum_{t=1}^{m} \frac{1}{\left[min\left(\left|\overline{P_{obst} P_{f(t)}}\right|, \left|\overline{P_{obst} P_{r(t)}}\right|\right) - d_{min}\right]} \tag{21}$$

where P_{obst} represents the coordinates of the nearest obstacle, and the selection of d_{min} ensures that $d_{min} > W + d/2$ to guarantee an adequate safety distance.

Motion stability: The vehicle's motion stability can be intuitively designed using the variation in pitch and roll angles along the trajectory. In the solution, $(\alpha, \varphi_f, \varphi_r)$ at each trajectory point can be estimated based on the contact point. Therefore, the evaluation function is constructed by calculating the changes in pitch and roll angles of the predicted posture at time t, specifically:

$$J_{stable}(i) = \sum_{t=1}^{m} c_1 \left(\alpha_{(t)} - \alpha_{(t-1)}\right) + c_2 \left[\left(\varphi_{f(t)} - \varphi_{f(t-1)}\right) + \left(\varphi_{r(t)} - \varphi_{r(t-1)}\right)\right] \tag{22}$$

where c_1 and c_2 are weighting factors. Typically, α reflects the steepness of the terrain, while φ_f and φ_r reflect its ruggedness. The difference between the two can be balanced in the emphasis of the evaluation function by varying c_1 and c_2 (accordingly)

Furthermore, due to the disparate dimensions and wide ranges of these sub-functions, we normalize them to ensure that each sub-function contributes to the total objective function in the predetermined proportion. This prevents any single sub-function from exerting an undue influence on the total objective function due to its large numerical range. By incorporating these sub-functions into a unified planning function according to different weighting factors, the complete expression can be formed below:

$$J(i) = \mu \frac{J_{heading}(i)}{\sum_{i=1}^{R} J_{heading}(i)} + \lambda \left(\frac{J_{dist}(i)}{\sum_{i=1}^{R} J_{dist}(i)}\right) + \delta \frac{J_{stable}(i)}{\sum_{i=1}^{R} J_{stable}(i)} \tag{23}$$

where R represents the total number of paths. The optimal trajectory is

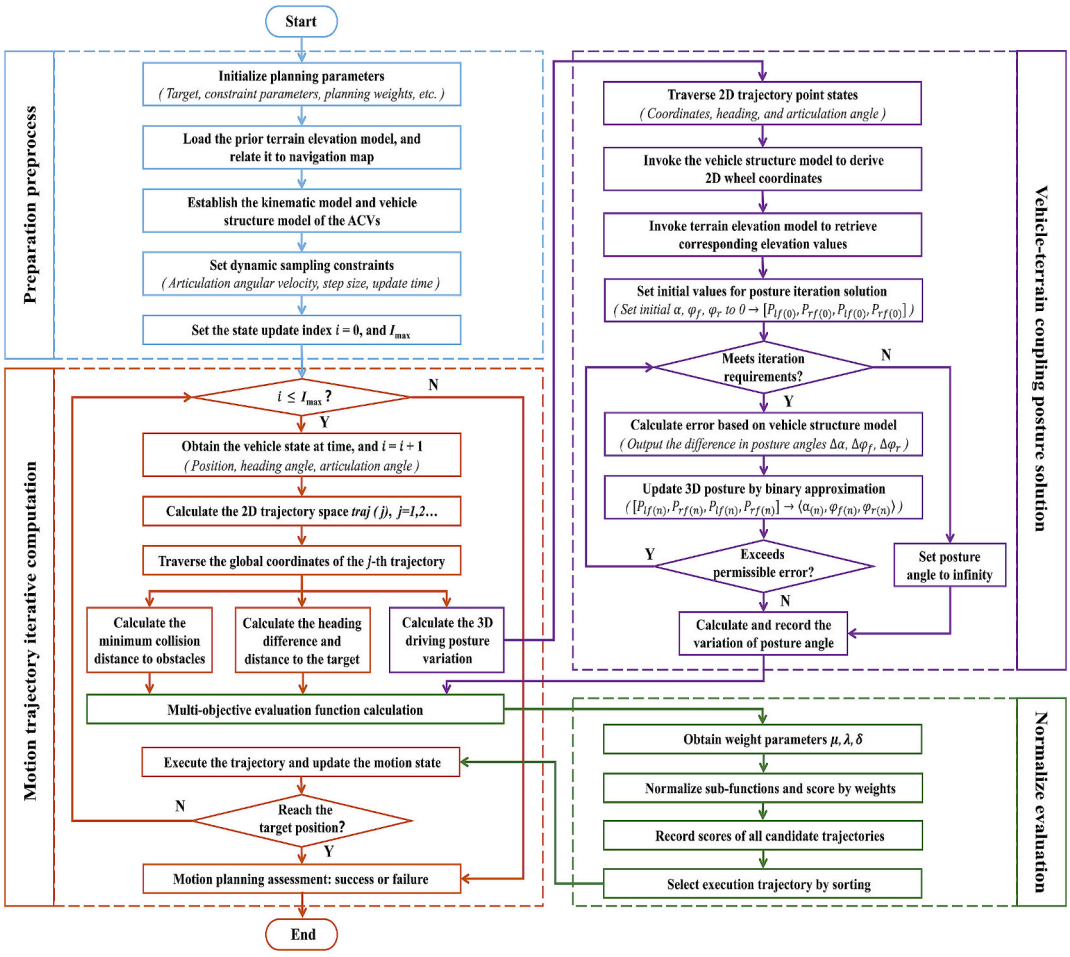

Fig. 7. Logical framework diagram of the overall algorithm.

determined by accumulating comparisons until $J(i) = J_{min}$. The weighting coefficients (μ, λ, δ) determine the relative importance of each objective in the total objective function.

This objective function is primarily designed for the effective determination of smooth trajectories in the vehicle-terrain coupling module. In practical applications, additional constraints such as acceleration and turning radius can be supplemented. Moreover, the positions of obstacles, target locations, and the vehicle's own state (such as velocity and angular velocity) are constantly changing in dynamic environments. Therefore, different weighting combinations can be employed to adjust the trajectories based on specific application scenarios and requirements. The experiments will be conducted to validate differences in trajectory solutions under various weighting combinations, suggesting more flexible strategies for adjusting planning expectations in practical applications.

3.6. Planner integration design

To ensure effective integration of the map model, motion primitives, coupled posture solver, and multi-objective evaluation within the motion planner, a systematic framework was designed based on the iterative mechanism to coordinate the interaction of these modules, as illustrated in Fig. 6. According to the real-time vehicle states, the planner first generates 2D candidate trajectories through the sampled window based on motion primitives. Then, these 2D trajectories are expanded into continuous 3D motion states using the coupled vehicle-terrain posture solver. Finally, both the 2D and 3D states of the candidate trajectories are evaluated using a multi-objective function to select the optimal trajectory for execution. This process is iteratively performed between the start and goal points, gradually accumulating short-term trajectories to form a complete motion path.

With this framework, the proposed motion planner can select the optimal motion primitives in real-time during vehicle movement, ensuring that ACVs smoothly reach the target location from the starting location through continuous trajectory connections. To align with this real-time dynamic planning mechanism, the planner algorithm is divided into four distinct functional components, as shown in Fig. 7. The functionality of these four components is described as follows:

Preparation preprocess: In this module, a priori terrain elevation models are imported to provide quantified environmental parameters for the planner. Concurrently, the kinematic model of articulated vehicles and a 3D structural model are established in advance to form the basis for computing vehicle motion trajectories.

Motion trajectory iterative computation: Serving as the planner's main function, this module iteratively computes, filters, and implements candidate vehicle trajectories based on a dynamic sampling window. The computation phase incorporates a vehicle-terrain coupling posture solution module to extend the representation of the vehicle's 3D posture along the driving trajectory. During the filtering phase, obstacle avoidance distances and travel distances are integrated under a normalized function designed for multi-objective evaluation to finalize trajectory scoring.

Vehicle-terrain coupling posture solution: This core functional module of the planner enables the perception of 3D motion trends, detailed in Section 3.4. It employs preloaded terrain elevation index models and vehicle 3D structural models to jointly calculate the

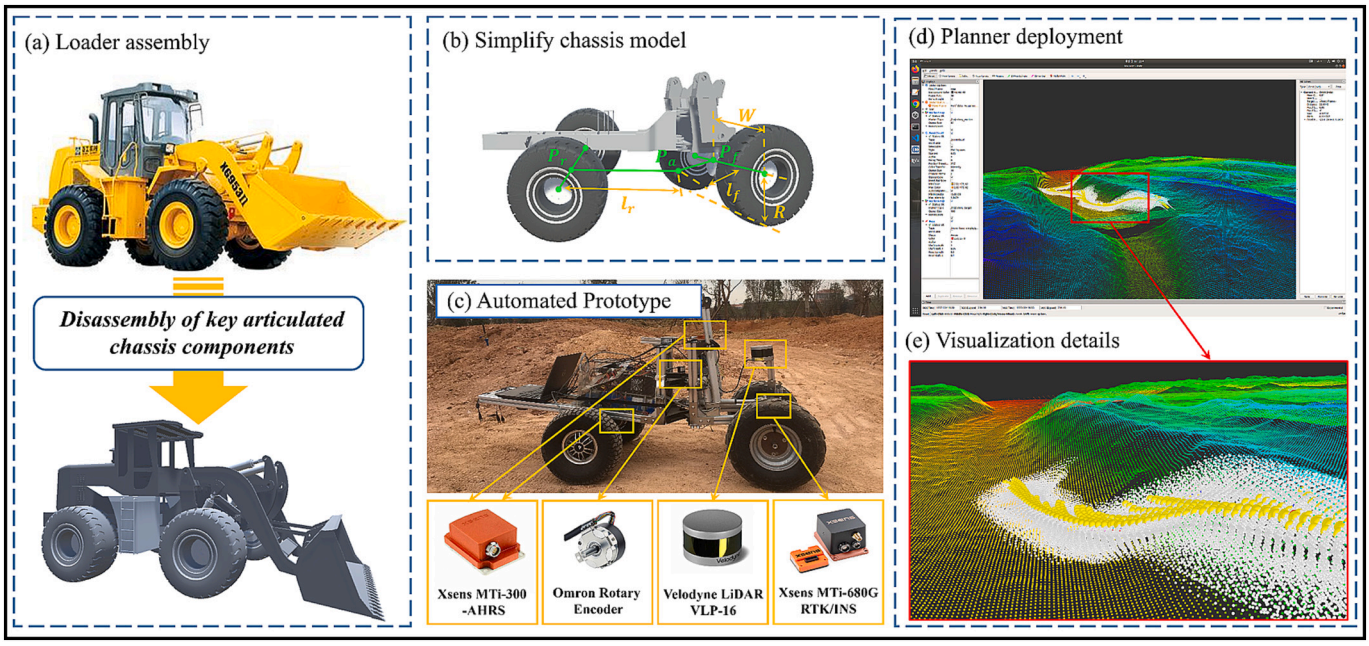

Fig. 8. Deployment of experimental prototype and planner.

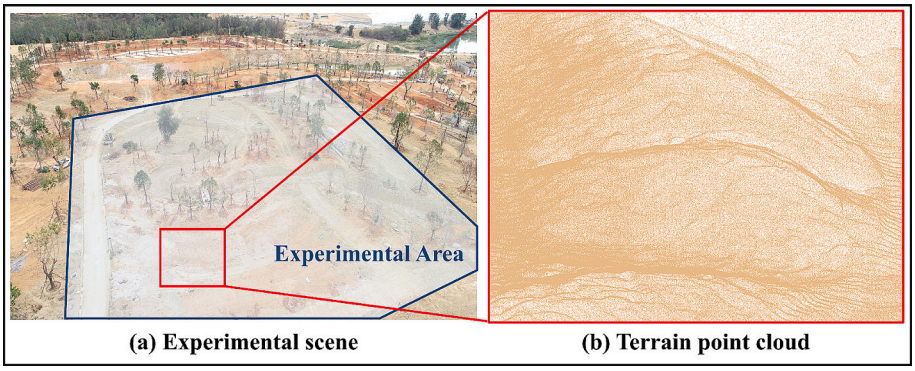

Fig. 9. Experimental scene and data.

grounding points of all four tires, thereby deriving changes in pitch and roll of the articulated vehicle body along the continuous trajectory.

Normalize evaluation: This module is responsible for the final trajectory selection. It normalizes parameters of different dimensions based on varying weights and selects execution trajectories based on their rankings.

During the planning process, trajectory data and vehicle states are primarily transferred and iterated in the form of arrays and matrix blocks, with data scale determined by the dynamic sampling window, step size, and update timing. Detailed real-time testing data is available in Table 5 of Section 5.3. It can be said that when deployed in actual systems, this planner exhibits high real-time performance, meeting the unmanned needs of low-speed engineering vehicles.

4. Implementation and deployment

4.1. ACV prototype platform

To evaluate and validate the proposed planner, a scale-down prototype with articulated chassis was deployed, which is shown in Fig. 8. Detailed vehicle parameters are provided in Table 1. The prototype's posture measurement system includes rotary encoders and RTK/INS. Rotary encoders at articulation points measure the angle, while the Xsens MTi-680G RTK/INS measures heading and position. The Xsens MTi-300-AHRS, installed at the rear axle pivot point and front vehicle body, measures body posture. A Velodyne VLP-16 LiDAR on the support pole captures terrain point cloud data.

The master computer utilizes the Ubuntu 18.04 operating system and is configured with an Intel i7-13650HX processor featuring 14 cores and a clock speed of 4.9 GHz, along with 32 GB of memory. Additionally, it is equipped with a Nvidia RTX4050 graphics card, possessing 6 GB of VRAM. The proposed planner is developed on the ROS platform integrated within the master computer and controls the prototype's movement via CAN communication. The prototype operates based on a well-established set of PID control logic. Notably, during the operation of the planner, the GPU is not utilized for computations; the CPU alone suffices to achieve rapid processing speeds.

4.2. Experimental scene and point cloud map

Fig. 9(a) shows the scene used for actual testing, which are early construction sites at the Xiang'an campus of Xiamen University. Fig. 9(b) shows a 3D point cloud map (83.27 m × 95.14 m) created by using drone aerial photography [48]. Through point cloud classification and filtering algorithms, few objects such as trees and weeds were removed from the map, retaining only the clear basic structure of the ground. The collected

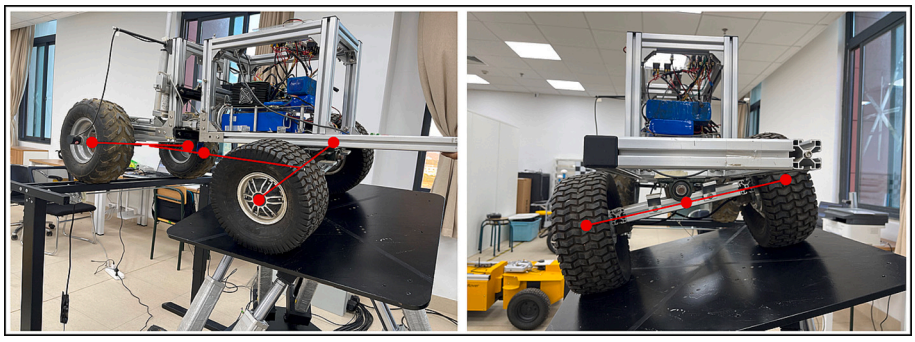

Fig. 10. Calibration experiment.

Table 2
Details and parameters of the compared planners.

Method	Category	Map type	Metrics	Validation
DEM-AIA	Graph search-based	DEM	Distance, posture angle, run-time	Simulation
T-Hybrid A*	Graph search-based	Hybrid map (Point cloud-based)	Distance, avoidance, posture angle	Field testing (Wheeled Robot)
Octo-RRT	Sampling-based	Octo map (3D model-based)	Distance, avoidance, posture angle	Field testing (Off-road vehicles)
BenchNav	Sampling-based	DEM	Distance, avoidance, Success rate	Simulation
Modified APF	Optimization-based	APF	Distance and Slope of waypoint	Field testing (Tracked robot)
Modified TEB	Optimization-based	3D model	Smoothness and Run-time	Simulation

point cloud contains a total of 9,367,717 points, averaging 1173 points per square meter. While ensuring accuracy for terrain settlement with tires, we down sampled appropriately to expedite solving the elevation index model [49].

4.3. Calibration of IMU mounted on vehicle

The IMUs installed on the front and rear vehicle bodies were calibrated using a designated 6-degree-of-freedom Stewart platform [50], as shown in Fig. 10. Comparing platform-recorded data with IMU measurements, we saw the repeat measurement errors of 1.05° for pitch and 0.86° for roll, which meet practical measurement needs. Additionally, validation was conducted for the maximum constraint angle for vehicle roll due to the limit block, confirmed at ±20°. Exceeding this angle difference between front and rear roll angles could cause the front wheels to lift off the ground, leading to out of control. Thus, during the planning process, this angle could serve as a cutoff point, with trajectory costs set to infinity when the front and rear roll angles differ over 20°.

4.4. Baseline of planner models

In terms of performance comparison of planners, we primarily investigated SOTA planning methods suitable for 3D unstructured environments that have been developed in recent years. The baselines and parameters of these methods are detailed in Table 2, sourced from the open-source community on GitHub. In terms of map inputs, we adjusted the input formats of the collected terrain point cloud models to match their map model inputs, such as artificial potential fields, 3D model, etc. Concurrently, we also modified the preset parameters of certain algorithms, such as Octo-RRT, BenchNav, and DEM-AIA, to ensure executability. The trajectories produced were analysed and compared through both simulation and actual vehicle operations.

5. Experimental results and analysis

In this section, the effectiveness of the proposed planner for ACVs operating on unstructured terrain is comprehensively analysed. Firstly, the accuracy metrics of the elevation index model are quantitatively evaluated in Section 5.1. Next, the prediction accuracy of ground contact points and vehicle attitude is validated by comparing data with model calculations in Section 5.2. Building on these, Section 5.3 validates the planner's overall performance under various weights and configuration parameters. Section 5.4 compares the planner's obstacle

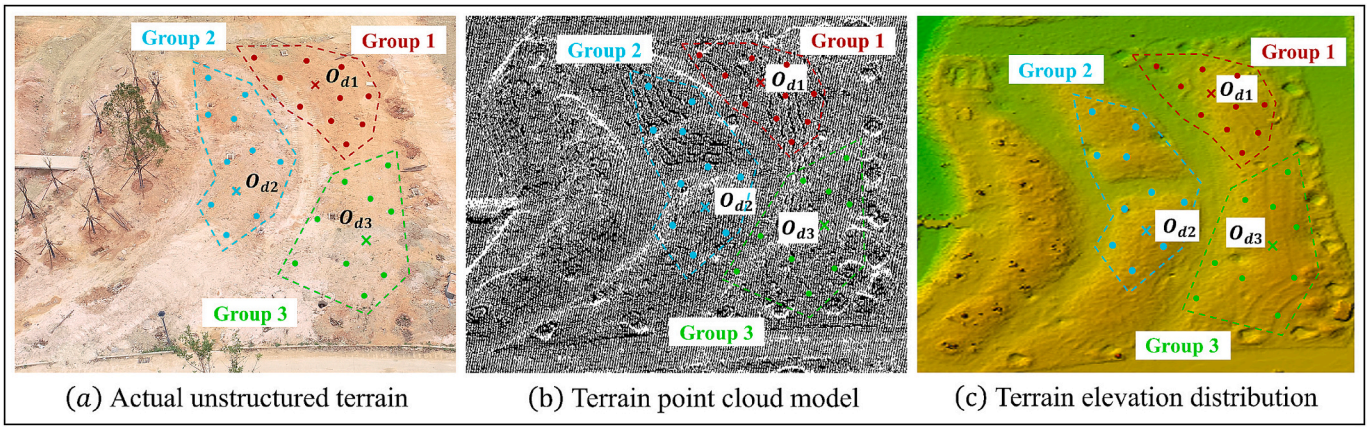

Fig. 11. Terrain mapping and measurement.

Table 3
Quantitative evaluation of terrain measurement errors.

Checkpoint group	Linear distance error			Elevation error		
	Mean	SE	RMSE	Mean	SE	RMSE
1	3.86	0.71	2.23	5.53	2.33	7.39
2	5.72	0.96	2.90	6.08	2.26	7.16
3	3.95	1.27	4.03	5.72	1.44	7.17
Average	4.51	0.58	3.31	5.78	1.13	6.50

avoidance capabilities and details. Finally, Section 5.5 offers a comprehensive comparison of the planner's terrain adaptability in actual scenarios.

5.1. Elevation map accuracy assessment

Fig. 11 shows the process of terrain mapping and measurement we conducted. More specifically, Fig. 11(a) shows actual unstructured terrain, Fig. 11(b) presents a terrain point cloud model, and Fig. 11(c) depicts terrain elevation distribution. We used a laser rangefinder to sequentially measure the actual distance values between each surveyed validation point and the reference point O_d, compared them with the point cloud map distance errors. Linear and elevation errors for each point were computed.

Table 3 shows the statistical results. As can be seen, the average linear distance error of three check point groups is 4.51 cm in both real-world environments and point cloud maps, meeting centimetre-level positioning accuracy standards. Moreover, in characterizing elevation discrepancies, the expected elevation error of the terrain index model for actual distance differences is 5.78 cm. The overall error distribution, as indicated by SE = 1.13 and RMSE = 6.50, shows a uniform distribution of errors, with higher error values primarily occurring in sparsely distributed point clouds. Considering prototype parameters, the maximum roll error caused by elevation errors is less than 5°, and the maximum pitch angle error is less than 3°, falling within an acceptable range for vehicle motion control errors.

5.2. Vehicle posture estimation accuracy

To evaluate the effectiveness of the vehicle-terrain coupling posture prediction method, we controlled our ACV moving at a speed of 1 m/s in the experimental terrain and recorded its motion trajectory that comprises 2D position coordinates from onboard GNSS, vehicle posture information from IMU, and angular information from the articulation point encoder, as shown in Fig. 12(a). Using these trajectory data, the tire contact points were determined for this segment of trajectory by using vehicle-terrain coupling solving module. Results in Fig. 12(c) and (d) demonstrate that the inferred tire contact points accurately conform to terrain changes, refining the actual motion trajectory of ACV prototype.

Furthermore, we compared ground attitudes with IMU-measured attitudes. Utilizing the vehicle attitude model from Section 3.4, we calculated pitch and front/rear roll angles. Fig. 13 shows a comparison

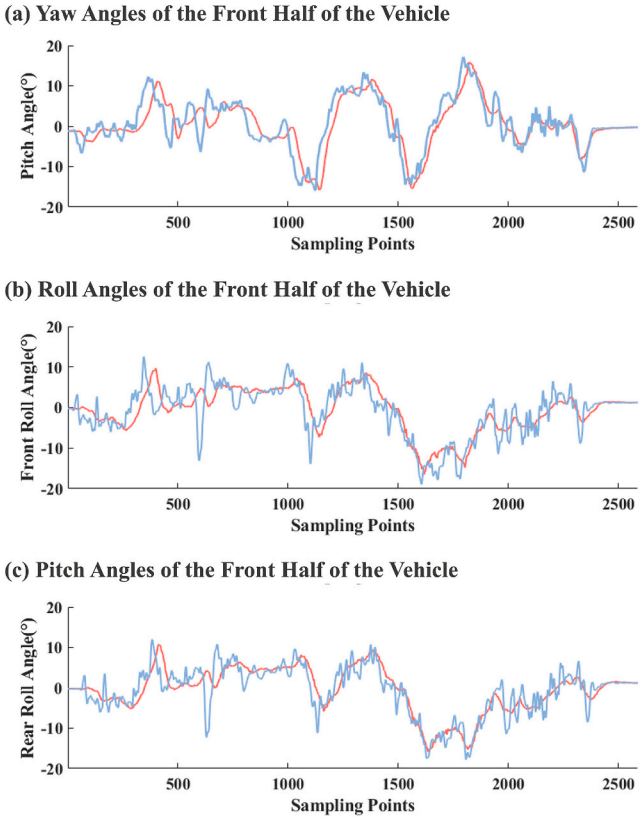

Fig. 13. Comparison of predicted posture with IMU measurement results.

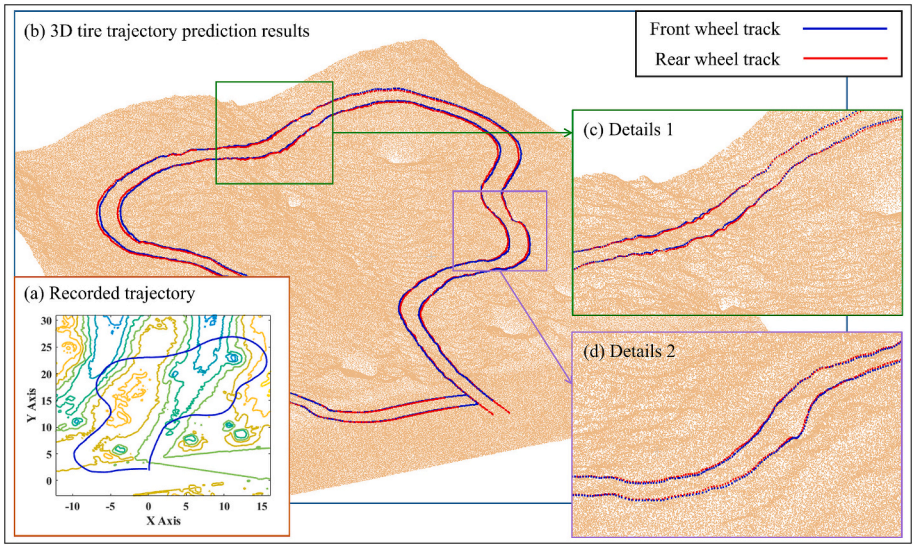

Fig. 12. Predicted results of wheel-ground contact points for motion trajectories.

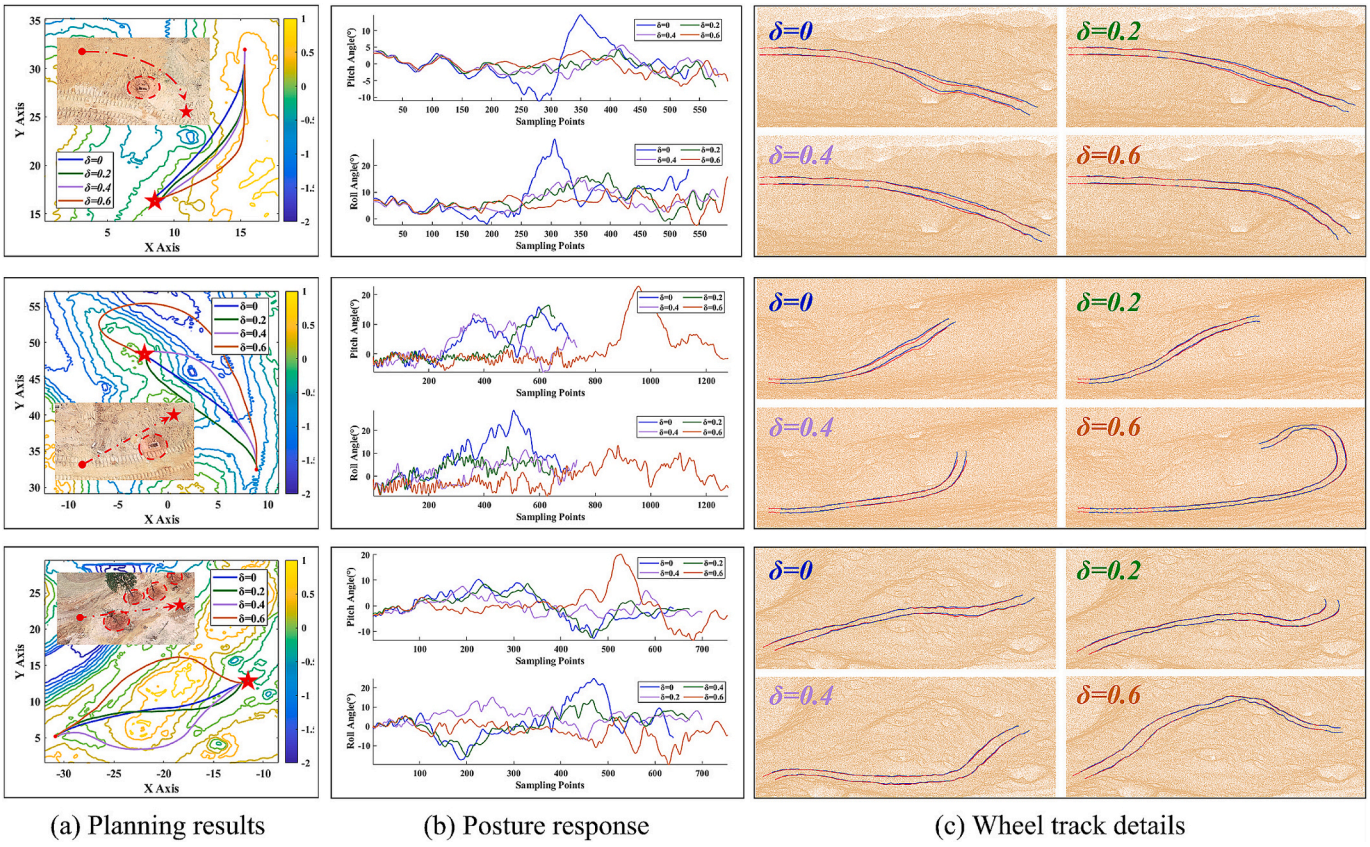

Fig. 14. Comparison of planning results under different stability weights.

Table 4
Performance metrics of planned trajectories under different stability weights.

Planner		Without terrain	With terrain		
Stability weight		δ=0	δ=0.2	δ=0.4	δ=0.6
Scene 1	Distance (m)	17.15	17.57	18.30	18.63
	Mean/max pitch (°)	4.11/14.69	2.73/ 6.86	1.98/ 5.64	1.87/ 6.69
	Mean/max roll (°)	11.54/29.94	7.17/ 17.26	6.61/ 15.56	5.72/ 15.81
Scene 2	Distance (m)	19.55	20.16	22.33	40.89
	Mean/max pitch (°)	5.76/15.98	3.84/ 16.44	4.68/ 13.71	3.95/ 22.91
	Mean/max roll (°)	9.38/28.81	4.32/ 13.02	4.05/ 11.53	4.22/ 13.51
Scene 3	Distance (m)	21.56	21.99	23.87	25.58
	Mean/max pitch (°)	4.61/12.65	3.58/ 12.29	2.65/ 7.61	3.91/ 20.12
	Mean/max roll (°)	8.89/24.68	5.15/ 15.68	5.02/ 15.14	3.95/ 19.83

of predicted postures with IMU measurement results. As can be seen, predicted trends closely matched measured results. To quantify errors, we sampled IMU data for uniform frequency, resulting average quantization errors of 5.53°, 6.21°, and 4.84°. Due to potential temporal matching errors, measured results might slightly overestimate over actual prediction errors. However, this does not affect our assessment of vehicle-terrain coupling attitudes. Overall, calculated attitude changes closely match actual motion trends, providing reasonably accurate predictions of vehicle travel attitudes on unstructured terrain.

5.3. *Planning performance evaluation*

To validate the effectiveness of the proposed motion planning algorithm, we conducted planning tests in typical unstructured environments with potholes, slopes, and obstacles. Fig. 14 shows a comparison of planning results under different stability weights. It reveals that planning trajectories without terrain influence considerations ($\delta = 0$) reach the destination by the shortest distance but overlook terrain-induced travel risks, evident in the severe jitter and rough trajectories of $\delta = 0$ as shown in Fig. 14(b) and Fig. 14(c). The proposed algorithm optimizes this local roughness phenomenon by setting different stability weights δ. For instance, trajectories with $\delta = 0.2$ and $\delta = 0.4$ sacrificed

Table 5
Planner real-time performance test results.

Sampling parameters			Single motion deduction			Iterative computation	
Steering resolutions(°)	Step sizes(s)	Predict range(s)	Trajectory points	Grounding points	Compute Time(ms)	Total trajectories	Total time(ms)
1	0.2	3	16	64	10.88	25	171.42
1	0.3	3	11	44	9.78	25	160.57
1	0.2	4	21	84	13.85	25	228.53
2	0.2	4	21	84	13.76	13	156.55

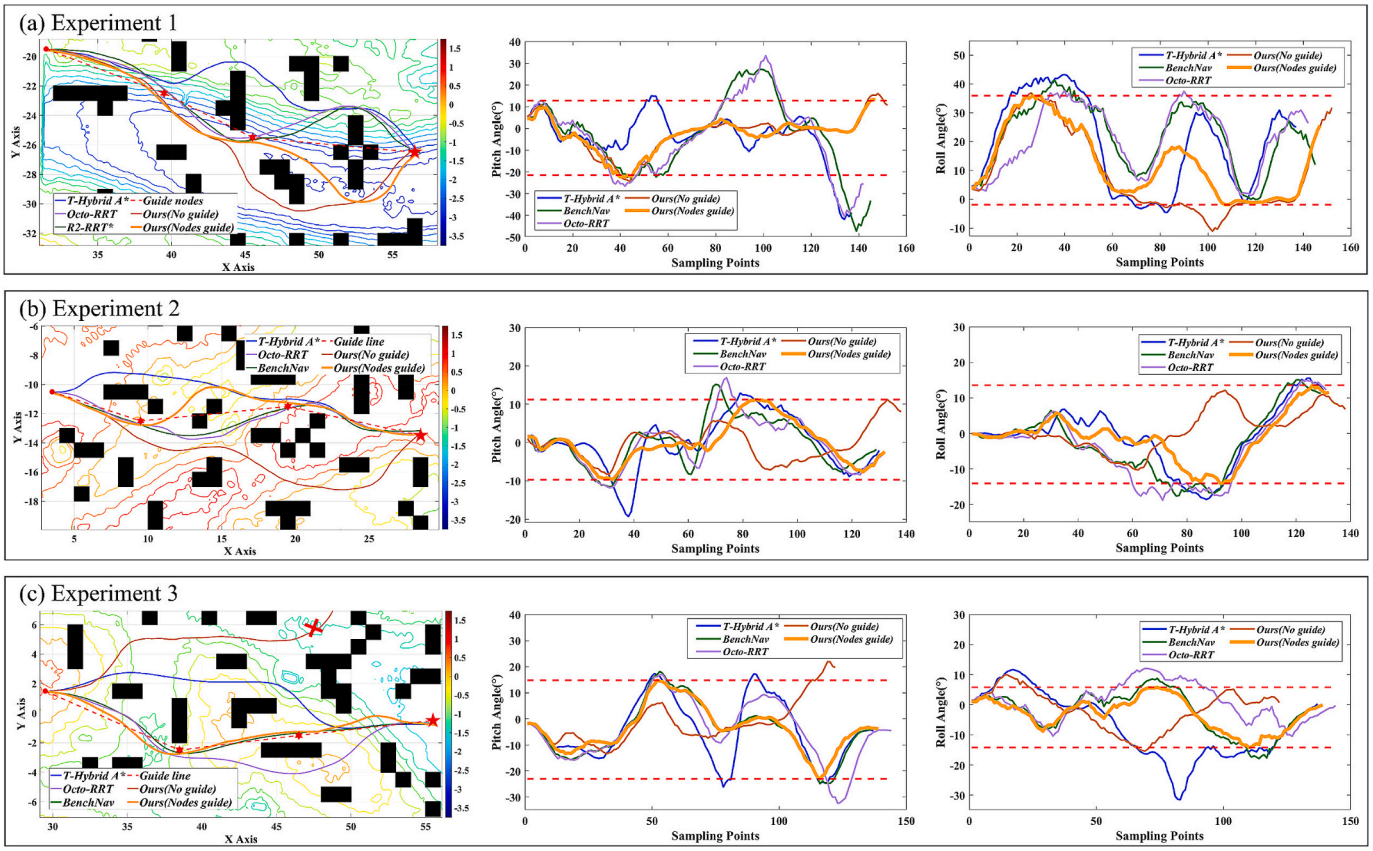

Fig. 15. Comparison of obstacle avoidance performance across different planner.

Table 6
Performance metrics of different obstacle avoidance trajectories.

Planner	T-Hybrid A*	Octo-RRT	BenchNav	Ours (No nodes)	Ours (Nodes guide)
Experiment 1 of Fig. 15(a)					
Distance (m)	**28.21**	28.72	28.84	30.64	29.78
Min avoid distance (m)	0.44	0.52	0.63	0.45	**0.80**
Mean/max pitch (°)	8.61/ 41.83	13.81/ 47.25	14.09/ 40.54	**5.97**/ 24.36	7.46/ **21.42**
Mean/max roll (°)	20.13/ 43.23	22.10/ 41.13	21.23/ 37.68	**14.86**/ **33.63**	16.49/ 35.91
Experiment 2 of Fig. 15(b)					
Distance (m)	**25.90**	26.19	26.30	27.68	26.50
Min avoid distance (m)	0.67	0.50	0.52	**0.72**	0.50
Mean/max pitch (°)	5.28/ 19.31	4.98/ 15.14	5.04/ 16.89	**4.18**/ **11.20**	5.03/ 11.61
Mean/max roll (°)	6.30/ 18.55	7.46/ 17.62	8.17/ 18.82	**4.38**/ **12.13**	4.71/ 14.07
Experiment 3 of Fig. 15(c)					
Distance (m)	27.38	**27.09**	28.80	–	27.81
Min avoid distance (m)	0.61	0.65	0.55	**0.76**	0.65
Mean/max pitch (°)	10.86/ 26.12	9.11/ 24.84	9.98/ 32.41	**6.65**/ **21.96**	7.62/ 22.98
Mean/max roll (°)	10.35/ 31.55	5.82/ 24.84	5.35/ 12.05	**4.01**/ 14.41	4.49/ **13.61**

travel distance to enhance ground contact smoothness to varying degrees. However, setting a higher smoothness weight did not always guarantee effectiveness. For instance, at $\delta = 0.6$, the algorithm initially prioritized trajectory smoothness in some scenarios, but made choices closer to the goal as travel progresses.

Combining IMU measured data, we further quantified the performance metrics of planned trajectories under different weight settings. Fig. 14(b) depicts actual data results, reflecting stability in early attitude angles at $\delta = 0.6$ but significant instability later. Hence, we prefer δ settings within [0.2, 0.4]. Table 4 shows the advantages of stabilizing vehicle roll angles at $\delta = 0.2$ and $\delta = 0.4$, with roll angle means mostly stable within 5° and maximum roll angles not exceeding 20°, with almost no abrupt changes. Although vehicle pitch angle variations are primarily terrain-dependent, the algorithm can stabilize pitch angles amidst undefined terrain features. Table 4 also shows the reduced average/maximum pitch angles compared to the original planned trajectories. Overall, in three typical scenarios, our proposed algorithm has significantly enhanced vehicle smoothness by slightly extending travel trajectories when δ is within [0.2, 0.4].

Furthermore, we conducted real-time tests under various parameter configurations to validate the computational efficiency of the planner. Notably, since the current prototype utilizes PID control, constraining speed can lead to control instability. Therefore, under the condition of constant speed, our algorithm primarily samples various steering resolutions, step sizes, and predict range. The articulated steering angle is constrained between [−27.5°, 27.5°], with angular acceleration and vehicle dynamic parameters available in Table 1. The planner's runtime on the ROS platform, as shown in Table 5, does not exceed 250 milliseconds under pure CPU operations. Considering the overall vehicle system's response delay, it can support up to a 3 Hz state update rate for real-time motion planning. However, given the low-speed characteristics of engineering vehicles, the algorithm typically samples using a 1°

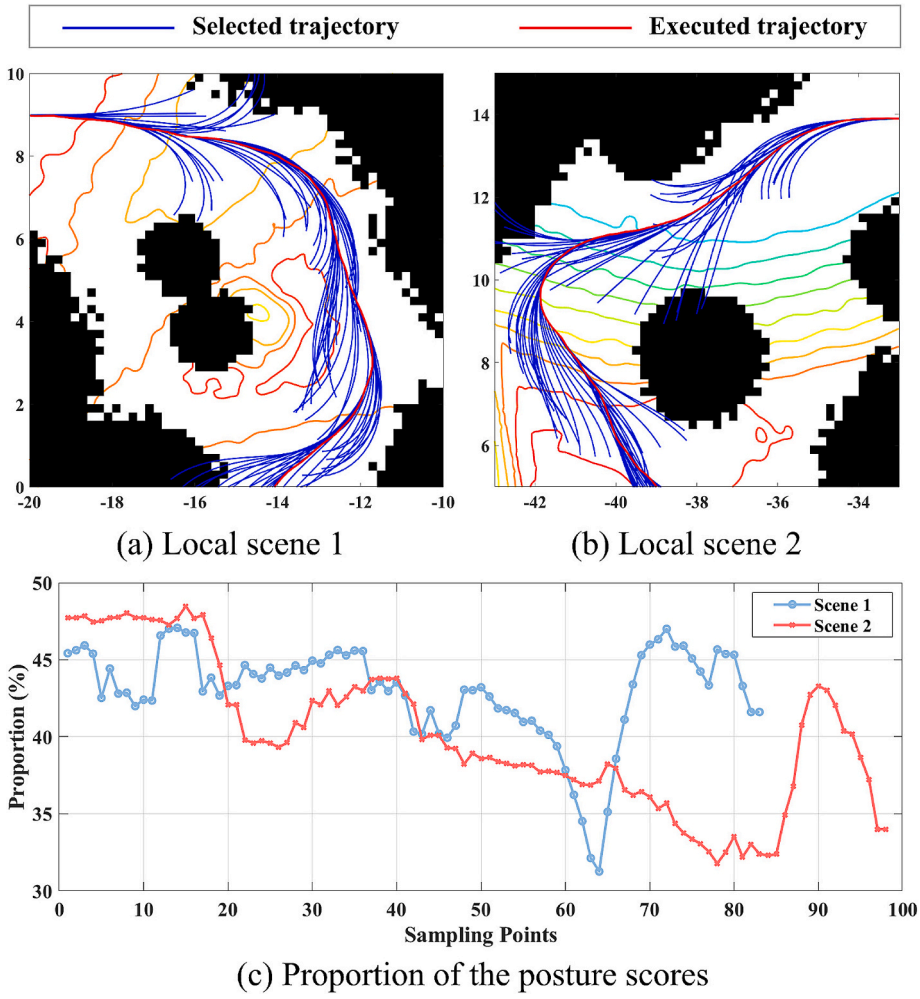

Fig. 16. Dynamic planning details in local scenarios.

resolution, 0.2 s step size, and 3 s prediction range, and employs a state update interval of 0.5 Hz to 1 Hz to maintain the effective execution of planned trajectories.

5.4. Comparative evaluation of obstacle avoidance

To evaluate the obstacle avoidance capabilities of our planner across various rugged terrains, we conducted comparative experiments on a randomly generated obstacle map with algorithms suited for 3D terrains: T-Hybrid A*, Octo-RRT, BenchNav, and our planner ($\delta = 0.3$). As depicted in Fig. 15, these algorithms, benefiting from the advantage of global traversal, all achieved distance-optimal obstacle avoidance trajectory planning. However, these methods focus solely on optimizing travel distance within a 3D space and do not adequately address the details of local travel stability, such as frequently navigating over slopes or pits with large posture angles. In contrast, our proposed planner prioritizes vehicle stability during local obstacle avoidance in terrains with multiple obstacles, which, in some instances, may lead to entrapment in dead zones, as shown in Fig. 15(c). Therefore, in complex obstacle environments, it is necessary to segment journeys under a global perspective, such as guiding the planner with key nodes from RRT. Results indicate that under the guidance of global nodes, our planner can also achieve a highly stable global trajectory by sacrificing some travel distance.

Table 6 displays the measurement indices for the trajectories. While T-Hybrid A*, Octo-RRT, BenchNav achieved globally optimal distances for 3D trajectories, they compromised the stability of average posture angles. In contrast, although our planner had a certain failure rate, its local trajectories were more stable. Moreover, according to the statistics in the table, under node guidance, our planner can afford an additional 1–3 m of travel per 30 m to reduce the average change in attitude angle by 2° to 8°. Additionally, integrating the data from Table 6 with trends from Fig. 16 reveals that in three obstacle avoidance scenarios, the highest pitch and roll angles occurred at locations with drastic terrain changes. Compared to other algorithms, our planner effectively reduced the maximum posture angles by increasing the obstacle clearance distance, thereby enhancing safety.

Furthermore, we detailed the trajectory selection specifics of our algorithm under two local scenes in Fig. 16(a) and (b), and quantitatively analysed the proportion of the posture scores relative to the total scores during the trajectory planning process in Fig. 16(c), thereby demonstrating the comprehensive assessment performance of the planner's evaluation function in local trajectory planning. Overall, the proportion of posture scores dynamically fluctuated throughout the evaluation, averaging approximately 40.13 % and 42.93 %. The motion trends depicted in Fig. 16(a) and (b) reveal that reductions in the posture score proportion primarily occur during deviations in course or proximity to obstacles. This indicates that the established scoring function is capable of effectively coordinating the dynamic relationships among multiple objectives in local planning.

5.5. Comparative evaluation and practical testing

To evaluate trajectory performance under distinctive design rules,

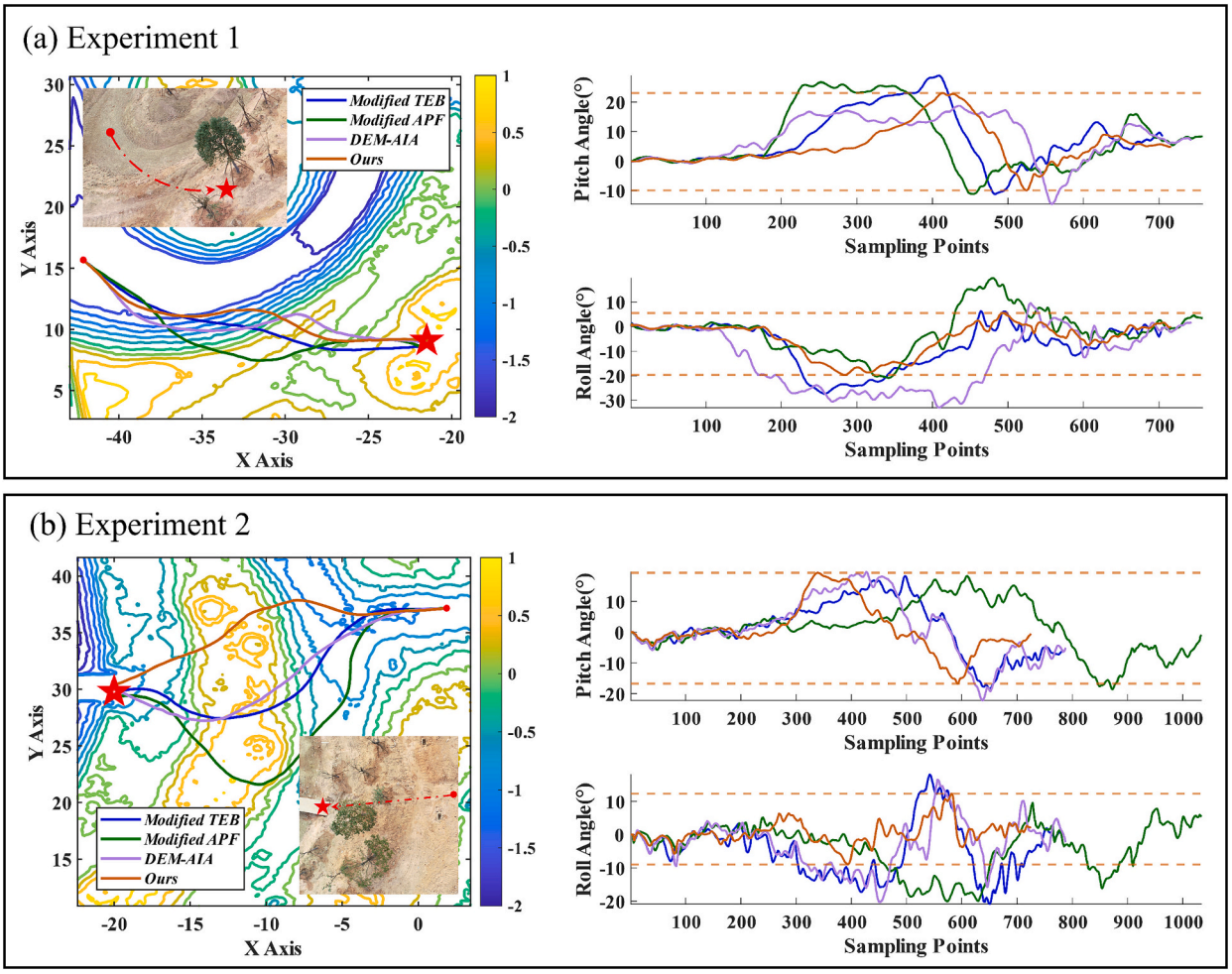

Fig. 17. Comparison of results from different planners.

Table 7
Comparison of performance metrics across different planner.

Planner	Modified TEB	Modified APF	DEM-AIA	Ours (δ=0.3)
Experiment 1 of Fig. 17(a)				
Distance (m)	23.62	25.81	25.43	**24.86**
Runtime (ms)	**2294**	2753	2301	5210
Explored nodes	**187**	364	251	473
Mean/max pitch (°)	6.48/27.35	8.66/**20.94**	9.34/32.95	**6.06**/23.08
Mean/max roll (°)	8.19/28.98	6.36/26.75	13.38/ 18.71	**5.42**/ **19.68**
Experiment 2 of Fig. 17(b)				
Distance (m)	43.68	59.29	47.25	**37.25**
Runtime (ms)	**2423**	2975	3865	6772
Explored nodes	**215**	481	363	589
Mean/max pitch (°)	7.08/**18.48**	6.38/18.58	7.41/22.16	**4.54**/19.31
Mean/max roll (°)	7.41/20.81	5.80/20.06	5.62/20.24	**3.62**/ **12.32**

our proposed algorithm was compared against three planning algorithms suitable for unstructured terrain. In steep slope environments depicted in Fig. 17(a), TEB, APF, and DEM-AIA adapted well to 3D terrain, maintaining trajectory smoothness in 3D space with fixed roll and pitch angles. However, this may pose risks in real-world scenarios as sudden loss of control in any attitude can lead risks to rollover. Our proposed algorithm adopted a strategy of gradual ascent to balance pitch and roll angles, effectively separating their high-value periods. It demonstrated advantages in slope traversal by not blindly avoiding obstacle weights but actively adjusting vehicle attitude through trajectory prediction based on motion models, as shown in Fig. 17(b).

Quantitative data in Table 7 highlights our algorithm's advantage in maintaining a dynamic balance between travel distance and attitude angles. Our proposed algorithm has demonstrated stable performance across different scenarios, particularly keeping the vehicle at gentle roll angles for most of the time (Mean Roll = 5.42° and 3.62°). However, this trajectory derivation was heavily reliant on model computation compared to TEB and APF, exhibiting low sensitivity to distance. Unlike TEB and APF, our algorithm's computation time accumulated with travel progress, favouring local planning over global planning.

Furthermore, we conducted tracking tests on these four planned paths using actual vehicles to verify their executability. Figs. 18 and 19 show that the motion trajectories derived from the proposed method exhibited superior tracking accuracy and speed stability compared to other methods. Repeated experiments reveal that the tracking error of ACVs on unstructured terrain was caused by the instability of vehicle speed and body attitude during steering.

6. Conclusions

In this paper, a motion planner is proposed to address the stability challenges of articulated construction vehicles (ACVs) operated on unstructured terrains. It can enhance the adaptability of ACVs to complex

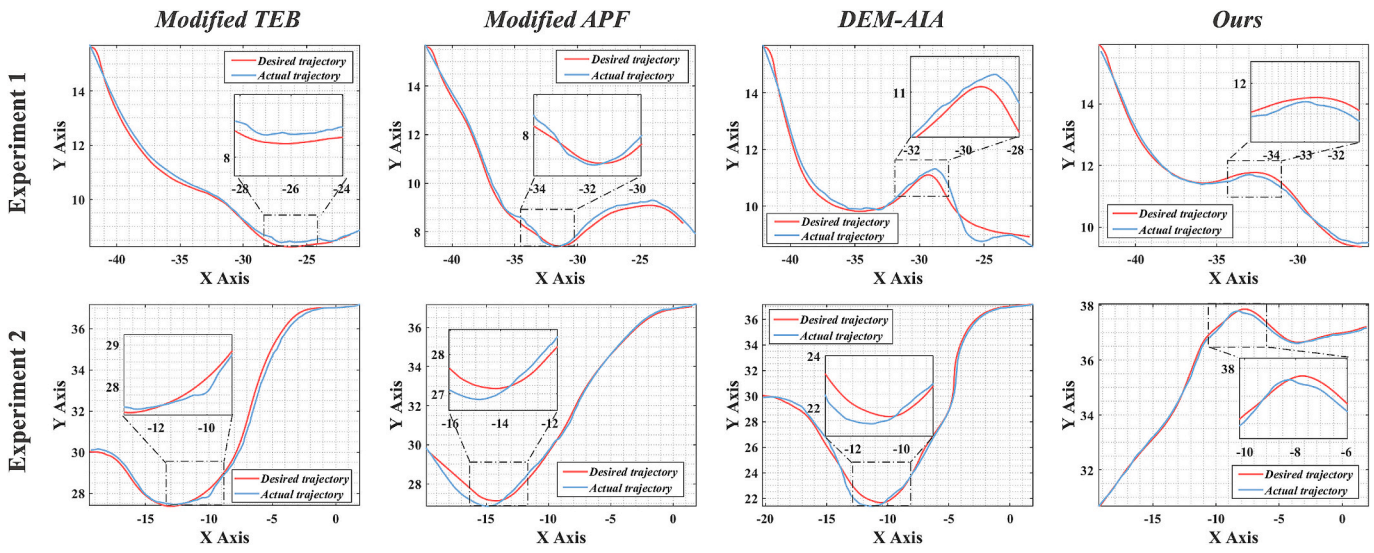

Fig. 18. Actual tracking errors in different scenarios.

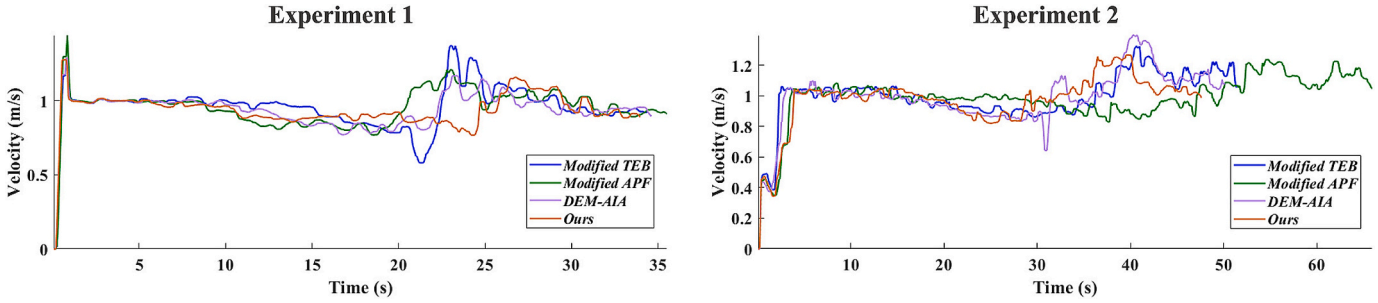

Fig. 19. Execution speed variation curve.

real-world environments by quantitatively evaluating terrain-vehicle interactions. Field experiments validate three key outcomes:

1) The planner's terrain excitation and vehicle response solver accurately forecasts the 3D motion postures of ACVs, providing the planner with quantifiable state information.
2) The planner's modular framework, which ties together trajectory sequences, posture representations, and evaluation functions, ensures that the system remains responsive while maintaining a streamlined workflow.
3) By normalizing weights across different evaluation objectives (travel distance, obstacle avoidance, and motion stability), the planner can dynamically balance competing priorities on a unified scale.

Despite its strengths, the planner has some limitations. Being based on the dynamic window approach, it lacks global environmental awareness, which can lead to local dead ends in obstacle-rich environments. Future work will focus on incorporating global guidance to better coordinate local and global planning objectives. Additionally, the current system is optimized for hard, unstructured surfaces and may struggle on muddy or soft terrain due to inaccuracies in posture prediction. Future research will explore new measurement methods to assess ground firmness and slip rates, enabling better performance on challenging terrain and improving the handling of fully loaded vehicles with high inertia.

References

[1] H.A. Nguyen, Q.P. Ha, Robotic autonomous systems for earthmoving equipment operating in volatile conditions and teaming capacity: a survey, Robotica 41 (2) (2023) 486–510, https://doi.org/10.1017/S0263574722000339.

[2] H. Ding, Z. Sang, Z. Li, J. Shi, Y. Wang, D. Meng, Trajectory planning and control of large robotic excavators based on inclination-displacement mapping, Autom. Constr. 158 (2024) 105209, https://doi.org/10.1016/j.autcon.2023.105209.

[3] T. Sardarmehni, X. Song, Path planning and energy optimization in optimal control of autonomous wheel loaders using reinforcement learning, IEEE Trans. Veh. Technol. 72 (8) (2023) 9821–9834, https://doi.org/10.1109/TVT.2023.3257742.

[4] B.R. Mantha, M.K. Jung, B.G. de Soto, C.C. Menassa, V.R. Kamat, Generalized task allocation and route planning for robots with multiple depots in indoor building environments, Autom. Constr. 119 (2020) 103359, https://doi.org/10.1016/j.autcon.2020.103359.

[5] R.O. Chavez-Garcia, J. Guzzi, L.M. Gambardella, A. Giusti, Learning ground traversability from simulations, IEEE Robot. Autom. Lett. 3 (3) (2018) 1695–1702, https://doi.org/10.1109/LRA.2018.2801794.

[6] J. Li, M. Ran, L. Xie, Efficient trajectory planning for multiple nonholonomic mobile robots via prioritized trajectory optimization, IEEE Robot. Autom. Lett. 99 (2020) 405–412, https://doi.org/10.1109/LRA.2020.3044834.

[7] A. Wang, A. Jasour, B.C. Williams, Non-gaussian chanceconstrained trajectory planning for autonomous vehicles under agent uncertainty, IEEE Robot. Autom. Lett. 5 (4) (2020) 6041–6048, https://doi.org/10.1109/LRA.2020.3010755.

[8] J. Yin, L. Li, Z.P. Mourelatos, Y. Liu, D. Gorsich, A. Singh, S. Tau, Z. Hu, Reliable global path planning of off-road autonomous ground vehicles under uncertain terrain conditions, IEEE Trans. Intell. Veh. (2023), https://doi.org/10.1109/TIV.2023.3317833.

[9] R. Oliveira, O. Ljungqvist, P.F. Lima, B. Wahlberg, Optimizationbased on-road path planning for articulated vehicles, IFAC-Pap. Onl. 53 (2) (2020) 15572–15579, https://doi.org/10.1016/j.ifacol.2020.12.2402.

[10] C. Jiang, Z. Hu, Z.P. Mourelatos, D. Gorsich, P. Jayakumar, Y. Fu, M. Majcher, R2-RRT*: reliability-based robust mission planning of off-road autonomous ground vehicle under uncertain terrain environment, IEEE Trans. Autom. Sci. Eng. 19 (2) (2021) 1030–1046, https://doi.org/10.1109/TASE.2021.3050762.

[11] Z. Liu, X. Yuan, G. Huang, W. Tan, Y. Wang, 3D gradient reconstruction-based path planning method for autonomous vehicle with enhanced roll stability, IEEE Trans. Intell. Transp. Syst. 23 (11) (2022) 20563–20571, https://doi.org/10.1109/TITS.2022.3177608.

[12] J. Markdahl, Automatic traction control for articulated off-road vehicles, IEEE Trans. Control Syst. Technol. 31 (2) (2022) 945–952, https://doi.org/10.1109/TCST.2022.3203194.

[13] Z. Xu, Y. Liu, L. Gan, X. Hu, Y. Sun, M. Liu, L. Wang, Csboundary: City-scale road-boundary detection in aerial images for highdefinition maps, IEEE Robot. Autom. Lett. 7 (2) (2022) 5063–5070, https://doi.org/10.1109/LRA.2022.3154052.

[14] D.D. Fan, A.-A. Agha-Mohammadi, E.A. Theodorou, Learning riskaware costmaps for traversability in challenging environments, IEEE Robot. Autom. Lett. 7 (1) (2021) 279–286, https://doi.org/10.1109/LRA.2021.3125047.

[15] P. Yang, M. Zang, H. Zeng, X. Guo, The interactions between an off-road tire and granular terrain: GPU-based DEM-fem simulation and experimental validation, Int. J. Mech. Sci. 179 (2020) 105634, https://doi.org/10.1016/j.ijmecsci.2020.105634.

[16] Z. Liu, X. Yuan, G. Huang, W. Tan, Y. Wang, 3D gradient reconstruction-based path planning method for autonomous vehicle with enhanced roll stability, IEEE Trans. Intell. Transp. Syst. 23 (11) (2022) 20563–20571, https://doi.org/10.1109/TITS.2022.3177608.

[17] H. Tian, B. Li, H. Huang, L. Han, Driving risk-aversive motion planning in off-road environment, Expert Syst. Appl. 216 (2023) 119426, https://doi.org/10.1016/j.eswa.2022.119426.

[18] B. Wu, Z. Chen, X. Lu, B. Xiao, A hierarchical model with hexagon grids for multi-objective route planning in large-scale off-road environments, Int. J. Geogr. Inf. Sci. 38 (7) (2024) 1388–1413, https://doi.org/10.1080/13658816.2024.2347319.

[19] A. Zou, L. Wang, W. Li, J. Cai, H. Wang, T. Tan, Mobile robot path planning using improved mayfly optimization algorithm and dynamic window approach, J. Supercomput. 79 (8) (2023) 8340–8367, https://doi.org/10.1007/s11227-022-04998-z.

[20] L. Liu, J. Lin, J. Yao, D. He, J. Zheng, J. Huang, P. Shi, Path planning for smart car based on dijkstra algorithm and dynamic window approach, Wirel. Commun. Mob. Comput. (2021) 1–12, https://doi.org/10.1155/2021/8881684.

[21] B. Wu, L. Hou, S. Wang, Y. Yin, S. Yu, Predictive modeling of loader's working resistance measurement based on multi-sourced parameter data, Autom. Constr. 149 (2023) 104805, https://doi.org/10.1016/j.autcon.2023.104805.

[22] D. Benz, J. Weseloh, D. Abel, H. Vallery, Ciot: Constraint-enhanced inertial-odometric tracking for articulated dump trucks in gnss-denied mining environments, in: 2023 IEEE International Conference on Robotics and Automation (ICRA), IEEE, 2023, pp. 10587–10593, https://doi.org/10.1109/ICRA48891.2023.10160664.

[23] Z. Chen, D. Wang, G. Chen, Y. Ren, D. Du, A hybrid path planning method based on articulated vehicle model, Comput. Mater. Contin 65 (2020) 1781–1793, https://doi.org/10.32604/cmc.2020.010902.

[24] Q. Zhang, R. Li, J. Sun, L. Wei, J. Huang, Y. Tan, Dynamic 3d pointcloud-driven autonomous hierarchical path planning for quadruped robots, Biomimetics 9 (5) (2024) 259, https://doi.org/10.3390/biomimetics9050259.

[25] C. Shen, S. Yu, B.I. Epureanu, T. Ersal, An efficient global trajectory planner for highly dynamical nonholonomic autonomous vehicles on 3D terrains, IEEE Trans. Robot. 40 (2023) 1309–1326, https://doi.org/10.1109/TRO.2023.3344030.

[26] Z. Chen, K. Chen, C. Song, X. Zhang, J.C. Cheng, D. Li, Global path planning based on BIM and physics engine for ugvs in indoor environments, Autom. Constr. 139 (2022) 104263, https://doi.org/10.1016/j.autcon.2022.104263.

[27] Z. Chen, H. Wang, K. Chen, C. Song, X. Zhang, B. Wang, J. Cheng, Improved coverage path planning for indoor robots based on BIM and robotic configurations, Autom. Constr. 158 (2024) 105160, https://doi.org/10.1016/j.autcon.2023.105160.

[28] A. Zhu, P. Pauwels, E. Torta, H. Zhang, B. De Vries, Data linking and interaction between bim and robotic operating system (ROS) for flexible construction planning, Autom. Constr. 163 (2024) 105426, https://doi.org/10.1016/j.autcon.2024.105426.

[29] J. Kim, D. Lee, J. Seo, Task planning strategy and path similarity analysis for an autonomous excavator, Autom. Constr. 112 (2020) 103108, https://doi.org/10.1016/j.autcon.2020.103108.

[30] Y. Wang, X. Liu, Z. Ren, Z. Yao, X. Tan, Synchronized path planning and tracking for front and rear axles in articulated wheel loaders, Autom. Constr. 165 (2024) 105538, https://doi.org/10.1016/j.autcon.2024.105538.

[31] H. Lee, W. Chung, A self-training approach-based traversability analysis for mobile robots in urban environments, in: 2021 IEEE International Conference on Robotics and Automation (ICRA), IEEE, 2021, pp. 3389–3394, https://doi.org/10.1109/ICRA48506.2021.9561394.

[32] H. Xue, H. Fu, L. Xiao, Y. Fan, D. Zhao, B. Dai, Traversability analysis for autonomous driving in complex environment: a lidarbased terrain modeling approach, J. Field Robot. 40 (7) (2023) 1779–1803, https://doi.org/10.1002/rob.22209.

[33] G.G. Waibel, T. Löw, M. Nass, D. Howard, T. Bandyopadhyay, P.V.K. Borges, How rough is the path? Terrain traversability estimation for local and global path planning, IEEE Trans. Intell. Transp. Syst. 23 (9) (2022) 16462–16473, https://doi.org/10.1109/TITS.2022.3150328.

[34] X. Cai, M. Everett, L. Sharma, P.R. Osteen, J.P. How, Probabilistic traversability model for risk-aware motion planning in off-road environments, in: 2023 IEEE/RSJ International Conference on Intelligent Robots and Systems (IROS), IEEE, 2023, pp. 11297–11304, https://doi.org/10.1109/IROS55552.2023.10341350.

[35] M. Toscano-Moreno, A. Mandow, M.A. Martínez, A. García-Cerezo, DEM-AIA: asymmetric inclination-aware trajectory planner for offroad vehicles with digital elevation models, Eng. Appl. Artif. Intell. 121 (2023) 105976, https://doi.org/10.1016/j.engappai.2023.105976.

[36] J. Liu, X. Chen, J. Xiao, S. Lin, Z. Zheng, H. Lu, Hybrid map-based path planning for robot navigation in unstructured environments, in: 2023 IEEE/RSJ International Conference on Intelligent Robots and Systems (IROS), IEEE, 2023, pp. 2216–2223, https://doi.org/10.1109/IROS55552.2023.10341666.

[37] Y. Ji, Y. Tanaka, Y. Tamura, M. Kimura, A. Umemura, Y. Kaneshima, H. Murakami, A. Yamashita, H. Asama, Adaptive motion planning based on vehicle characteristics and regulations for off-road ugvs, IEEE Trans. Industr. Inform. 15 (1) (2018) 599–611, https://doi.org/10.1109/TII.2018.2870662.

[38] M. Endo, K. Honda, G. Ishigami, Benchnav: Simulation platform for benchmarking off-road navigation algorithms with probabilistic traversability, arXiv preprint (2024), https://doi.org/10.48550/arXiv.2405.13318.

[39] J. Hu, Y. Hu, C. Lu, J. Gong, H. Chen, Integrated path planning for unmanned differential steering vehicles in off-road environment with 3d terrains and obstacles, IEEE Trans. Intell. Transp. Syst. 23 (6) (2021) 5562–5572, https://doi.org/10.1109/TITS.2021.3054921.

[40] M. Chen, S.L. Herbert, H. Hu, Y. Pu, J.F. Fisac, S. Bansal, S. Han, C.J. Tomlin, Fastrack: a modular framework for real-time motion planning and guaranteed safe tracking, IEEE Trans. Autom. Control 66 (12) (2021) 5861–5876, https://doi.org/10.1109/TAC.2021.3059838.

[41] Y. Qi, B. He, R. Wang, L. Wang, Y. Xu, Hierarchical motion planning for autonomous vehicles in unstructured dynamic environments, IEEE Robot. Autom. Lett. 8 (2) (2022) 496–503, https://doi.org/10.1109/LRA.2022.3228159.

[42] M. Yao, H. Deng, X. Feng, P. Li, Y. Li, H. Liu, Improved dynamic windows approach based on energy consumption management and fuzzy logic control for local path planning of mobile robots, Comput. Ind. Eng. 187 (2024) 109767, https://doi.org/10.1016/j.cie.2023.109767.

[43] D. Chen, M. Zhuang, X. Zhong, W. Wu, Q. Liu, Rspmp: Realtime semantic perception and motion planning for autonomous navigation of unmanned ground vehicle in off-road environments, Appl. Intell. 53 (5) (2023) 4979–4995, https://doi.org/10.1007/s10489-022-03283-z.

[44] L. Heng, D. Yifan, Z. Xinran, L. Haiyi, J. Jianmin, Z. Yanyong, OCC-VO: Dense mapping via 3d occupancy-based visual odometry for autonomous driving, arXiv: 2309.11011v2 (2023), https://doi.org/10.48550/arXiv.2309.11011.

[45] S. Song, T. Huang, C. Li, G. Shao, Y. Gao, Q. Zhu, A safetyassured semantic map for an unstructured terrain environment towards autonomous engineering vehicles, Drones 7 (9) (2023) 550, https://doi.org/10.3390/drones7090550.

[46] F. Dou, Y. Huang, L. Liu, H. Wang, Y. Meng, L. Zhao, Path planning and tracking for autonomous mining articulated vehicles, Int. J. Heavy Veh. Syst. 26 (3–4) (2019) 315–333, https://doi.org/10.1504/IJHVS.2019.101475.
[47] D. Lee, S. Lee, C. Ahn, P. Shi, C. Lim, Finite distribution estimation-based dynamic window approach to reliable obstacle avoidance of mobile robot, IEEE Trans. Ind. Electron. 68 (10) (2020) 9998–10006, https://doi.org/10.1109/TIE.2020.3020024.
[48] C. Yang, M. Tsai, S. Kang, C. Hung, UAV path planning method for digital terrain model reconstruction–a debris fan example, Autom. Constr. 93 (2018) 214–230, https://doi.org/10.1016/j.autcon.2018.05.024.
[49] J. Chen, L. Xiong, B. Yin, G. Hu, G. Tang, Integrating topographic knowledge into point cloud simplification for terrain modelling, Int. J. Geogr. Inf. Sci. 37 (5) (2023) 988–1008, https://doi.org/10.1080/13658816.2023.2180801.
[50] V.S. Arconada, J. García-Barruetabeña, R. Haas, Validation of a ride comfort simulation strategy on an electric Stewart platform for real road driving applications, J. Low Freq. Noise Vib. Act. Control 42 (1) (2023) 368–391, https://doi.org/10.1177/14613484221122109.